Dropsonde Observations in Low-Level Jets over the Northeastern Pacific Ocean from CALJET-1998 and PACJET-2001: Mean Vertical-Profile and Atmospheric-River Characteristics

F. MARTIN RALPH AND PAUL J. NEIMAN

NOAA/Environmental Technology Laboratory, Boulder, Colorado

RICHARD ROTUNNO

National Center for Atmospheric Research, Boulder, Colorado

(Manuscript received 15 April 2004, in final form 17 September 2004)

ABSTRACT

Dropsonde observations are used to document the mean vertical profiles of kinematic and thermodynamic conditions in the pre-cold-frontal low-level-jet (LLJ) region of extratropical cyclones over the eastern Pacific Ocean. This is the region within storms that is responsible not only for the majority of heavy rainfall induced by orography when such storms strike the coast, but also for almost all meridional water vapor transport at midlatitudes. The data were collected from NOAA's P-3 aircraft in 10 storms during the California Land-falling Jets Experiment (CALJET) of 1998 and in 7 storms during the Pacific Land-falling Jets Experiment (PACJET) of 2001. The mean position of the dropsondes was 500 km offshore, well upstream of orographic influences. The availability of data from two winters that were characterized by very different synoptic regimes and by differing phases of ENSO—that is, El Niño in 1998 and La Niña in 2001—allowed examination of interannual variability.

The composite pre-cold-frontal profiles reveal a well-defined LLJ at 1.0-km altitude with a wind speed of 23.4 m s^{-1} and a wind direction of 216.7°, as well as vertical shear characteristic of warm advection. The composite thermodynamic conditions were also documented, with special attention given to moist static stability due to the nearly saturated conditions that were prevalent. Although the dry static stability indicated very stable conditions (4.5 K km^{-1}), the moist static stability was approximately zero up to 2.8-km altitude. Although the composite winds, temperatures, and water vapor mixing ratios in 2001 differed markedly from 1998, the moist static stability remained near zero from the surface up to 2.8–3.0-km altitude for both seasons. Hence, orographic precipitation enhancement is favored in this sector of the storm, regardless of the phase of ENSO.

The dropsonde data were also used to characterize the depth and strength of atmospheric rivers, which are responsible for most of the meridional water vapor transport at midlatitudes. The vertically integrated along-river water vapor fluxes averaged 525×10^5 kg s^{-1} (assuming a 100-km-wide swath), while the meridional and zonal components were 387×10^5 kg s^{-1} and 302×10^5 kg s^{-1}, respectively. Although the composite meridional transport in 2001 was less than half that in 1998 (230×10^5 kg s^{-1} versus 497×10^5 kg s^{-1}), the characteristic scale height of the meridional water vapor transport remained constant; that is, 75% of the transport occurred below 2.25-km altitude.

1. Introduction

Precipitation resulting from the landfall of extratropical cyclones on the U.S. West Coast is both a critical source for water supply and a cause of flooding. Knowledge of the physical processes that cause this precipitation is critical to improving quantitative precipitation forecasting (QPF) in the region and to understanding the linkages between weather and climate in the water cycle. Forecasters and scientists have long known that a key feature that determines both the location and intensity of rainfall in such storms on the West Coast is the pre-cold-frontal low-level jet (LLJ). The LLJ is an integral part of extratropical cyclones and is characterized by warm temperatures, weak stratification, large water vapor content, and strong low-altitude winds (e.g., Browning and Pardoe 1973). These attributes are conducive to the production of heavy rainfall through orographic forcing when the LLJ strikes the coastal mountains.

In an effort to improve understanding of the role of

Corresponding author address: F. Martin Ralph, NOAA/Environmental Technology Laboratory, Mail Code R/ET7, 325 Broadway, Boulder, CO 80305.
E-mail: Marty.Ralph@noaa.gov

the pre-cold-frontal LLJ and associated orographic precipitation processes in QPF, the California Land-falling Jets Experiment (CALJET; Ralph et al. 1999) was conducted along and offshore of the California coast during the winter of 1997/98, a year that was characterized by a very strong El Niño. The follow-on Pacific Land-falling Jets Experiment (PACJET-01) in the winter of 2000/01 extended this effort to more of the U.S. West Coast and to a season influenced by weak La Niña conditions. Dropsonde data collected offshore by the National Oceanic and Atmospheric Administration's (NOAA) P-3 research aircraft in 17 storms during these two winters are the focus of this paper. [A second phase of PACJET was conducted in the winter of 2001/02 (PACJET-02), but did not have flight objectives that allowed for collection of dropsonde data that were of use in this study.] The analyses presented here build on several recent CALJET studies concerning the LLJ based on coastal observations from wind profilers, vertically pointing S-band radars, rain gauges and stream gauges, and offshore aircraft and satellite observations. Specifically, Neiman et al. (2002) documented the influence of wind speed and blocking in controlling orographic and coastal rainfall, Ralph et al. (2003) and Andrews et al. (2004) described the influence of wind direction on both rainfall and runoff, White et al. (2003) found that microphysical conditions varied with wind direction, and Ralph et al. (2004) documented aspects of narrow regions of strong horizontal water vapor transport.

Orographic enhancement of rainfall along windward coasts has long been noted in the literature (e.g., Bjerknes and Solberg 1921; Douglas and Glasspoole 1947; Bergeron 1965; Nordø and Hjortnæs 1966; Browning 1980; Neiman et al. 2002). A central element in both the understanding and prediction of this effect is a knowledge of the vertical motion induced as air flowing toward a coast tries to pass over (or around) coastal orography since, in cases of thermodynamically stable air masses, such knowledge leads directly to an estimate of the total condensation (Sawyer 1956). Recently, Neiman et al. (2002) used extensive coastal wind profiler and rain gauge data from CALJET to extend greatly the documentation of the critical role of upslope wind speed in determining rain rates in coastal mountains and revealed the importance of blocking by the terrain in increasing rainfall at the base of the windward slope. They also showed that orographic precipitation efficiency was 50% greater when an LLJ was present than when one was not (i.e., for a unit increase in the magnitude of upslope flow, the rain-rate increase is 50% greater in LLJ conditions). This likely results from a combination of factors, including the higher water vapor content often associated with LLJs and potentially the presence of weaker static stability. As orographically induced vertical motion depends critically on the upstream atmospheric stability (e.g., Colle 2004), a determination of the latter, including effects of moisture, is important to examine. In spite of its importance, there have been only a few studies (see the review by Smith 1979) that have reported even limited measurements of the thermodynamic profiles upwind of coastal orography associated with enhanced rainfall. In the present study, a subset of the 284 dropsondes released over the Pacific Ocean during the CALJET and PACJET-01 field experiments (Fig. 1) is used to analyze the thermodynamic stability of the air masses upwind of the California coastal orography that are responsible for intense coastal rainfall, that is, the LLJ in extratropical cyclone warm sectors. Because CALJET and PACJET-01 targeted the LLJ using the NOAA P-3 aircraft over two winters, the dropsonde data provide a unique opportunity to examine conditions in this critical air mass.

While the above-referenced studies and objectives of this paper focused on the conditions created by the landfall of LLJs, Ralph et al. (2004) documented key elements of its structure offshore. This was accomplished using a combination of a detailed case study based upon P-3 dropsonde data in one event and a winter-season composite created from satellite data and National Centers for Environmental Prediction–National Center for Atmospheric Research (NCEP–NCAR) reanalyzes in many events through the winter of 1997/98. While the case study revealed the full vertical structure of moisture [including integrated water vapor (IWV)] across a pre-cold-frontal LLJ, the satellite compositing focused on the lateral structure of IWV. (The composite results confirmed the representativeness of the single case study in terms of the width scales, but was unable to address the representativeness of the depth scale.) Because of the critical role the LLJ plays in transporting water vapor, both in terms of precipitation and flood prediction, and its role in the global water cycle, Ralph et al. (2004) focused on the meridional water vapor transport. Because the region of strongest water vapor transport was found to be very narrow, and yet is responsible for almost all of the meridional water vapor transport at midlatitudes (Zhu and Newell 1998), this region is referred to as an "atmospheric river" (Zhu and Newell 1998; Ralph et al. 2004). Although Ralph et al. (2004) clearly documented several key attributes of atmospheric rivers by compositing satellite data, they were unable to quantify the mean vertical profile of conditions in atmospheric rivers, and they examined only one season. The present paper fills this gap by using dropsonde observations from 17 flights during which aircraft data were collected when a pre-cold-frontal LLJ was present offshore (Fig. 1; Table 1). In addition to the full 2-yr composite, means derived from only the El Niño winter of 1997/98 and from the La Niña winter of 2001 are compared to document interannual variability.

In short, when an atmospheric river impacts coastal mountains, the detailed spatiotemporal distribution of orographic effects transforms the horizontal water va-

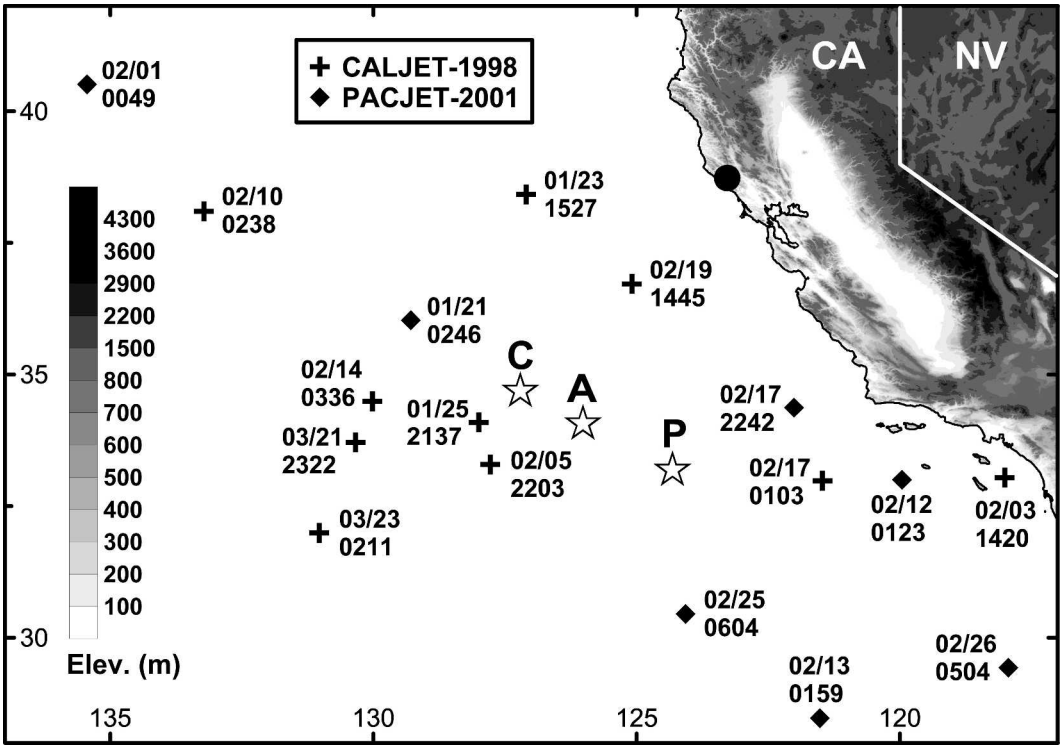

FIG. 1. Base map of California and vicinity showing gray-shaded terrain (m) and the locations of the 17 pre-cold-frontal dropsondes used in this study. Ten of these dropsondes were deployed in 1998 during CALJET and the remaining seven were deployed in 2001 during PACJET-01 (see inset key). The month/day (MM/DD) and time (UTC) of the dropsondes are shown next to their respective locations. The average positions of the 10 CALJET dropsondes, 7 PACJET dropsondes, and all 17 dropsondes are shown with stars next to a bold "C," "P," and "A," respectively. The location of the microphysics site at Cazadero is shown with a bold black dot.

por transport into enhanced rainfall and ultimately runoff. This paper strives to fill key gaps in current knowledge of the mean conditions within these atmospheric rivers upstream of coastal effects, both in terms of the vertical structure of the water vapor transport and in terms of the vertical profiles of the basic thermodynamic and kinematic characteristics that ultimately govern the atmosphere's response to orography when this airstream strikes coastal mountains.

Section 2 describes the key observing systems. Methodolgies are described in section 3. Dropsonde results for the two full winters are shown in section 4. Variations between the CALJET and PACJET composites are described in section 5, and conclusions are presented in section 6.

2. Observing systems

a. The airborne data-collection strategy

During the winters of 1997/98 and 2000/01, an extensive suite of research observing platforms were deployed for CALJET and PACJET-01 across a region covering the data-sparse eastern Pacific Ocean and coastal California (Ralph et al. 1999; White et al. 2002). This suite included a NOAA P-3 turboprop research aircraft (e.g., Jorgensen and Smull 1993; Jorgensen et al. 1996) that measured standard flight-level meteorological parameters every 1 s using in situ sensors and high-resolution vertical profiles of wind velocity, temperature, and water vapor using global positioning system (GPS) dropsondes manufactured by Vaisala. A total of 196 dropsondes were released over the eastern Pacific during CALJET, and 88 dropsondes were released in the same region during PACJET-01. Most of these were deployed outside the LLJ itself as part of joint targeted dropsonde efforts with NCEP and the Naval Research Laboratory in 1998 [North Pacific Experiment (NORPEX); Langland et al. 1999] and NCEP in 2001 (Winter Storms Reconnaissance Program; Szunyogh et al. 2002). However, a number of dropsondes were deployed directly into pre-cold-frontal LLJs, a subset of which (one per storm) is used here. As is described fully in section 3a, this resulted in 10 and 7 dropsondes from CALJET and PACJET-01, respectively, that were well suited to this study. The locations, dates, and times of these dropsondes are shown in Fig. 1 and Table 1. The P-3's primary operating altitude when these dropsondes were deployed was between 450 and 500 mb. Of the 43 P-3 flights conducted during CALJET and PACJET-01, roughly half had mission

TABLE 1. The dates, times, and locations of the 17 dropsondes, and key observations from these dropsondes. Companion information for the CALJET, PACJET, 17-case composites is also shown.

Year	Month	Day	Hour (UTC)	Lat (°N)	Lon (°W)	1.0 km speed (m s^{-1})	1.0 km direction (^{O})	IWV (cm)	Vertically integrated horizontal moisture flux (10^5 kg s^{-1})		
									Zonal	Meridional	Along-river
1998	Jan	23	1527	38.42	127.10	30.5	210.4	2.78	443	628	765
1998	Jan	25	2137	34.09	128.00	21.8	216.8	2.27	259	222	332
1998	Feb	03	1420	33.04	118.01	30.0	156.2	2.64	−133	642	642
1998	Feb	05	2203	33.29	127.78	36.5	194.8	2.70	305	795	847
1998	Feb	10	0238	38.10	133.22	40.5	220.4	2.39	498	674	836
1998	Feb	14	0336	34.49	130.02	29.3	258.8	3.33	860	291	901
1998	Feb	17	0103	32.98	121.47	16.6	213.2	2.03	243	218	315
1998	Feb	19	1445	36.72	125.09	23.3	230.2	2.13	334	327	465
1998	Mar	21	2322	33.71	130.34	30.1	223.2	3.22	609	671	890
1998	Mar	23	0211	31.99	131.03	26.6	221.5	2.62	411	506	652
2001	Jan	21	0246	36.03	129.29	22.2	181.1	2.52	53	473	474
2001	Feb	01	0049	40.51	135.44	26.8	211.7	2.61	375	442	573
2001	Feb	12	0123	33.00	119.96	9.2	226.6	1.75	168	92	185
2001	Feb	13	0159	28.47	121.52	21.0	226.7	2.01	322	235	395
2001	Feb	17	2242	34.37	122.01	11.9	190.8	2.14	25	270	270
2001	Feb	25	0604	30.45	124.07	13.3	265.4	2.44	256	27	258
2001	Feb	26	0504	29.43	117.94	7.2	235.3	1.95	97	69	119
CALJET 10-case composite				34.68	127.21	28.5*	214.5*	2.61	383**	497**	664**
PACJET 7-case composite				33.18	124.32	15.9*	219.7*	2.20	185**	230**	325**
Full 17-case composite				34.06	126.02	23.4*	216.7*	2.44	302**	387**	525**

* Vector means derived from the 17 individual soundings.
** Vertically integrated fluxes derived from the composite soundings rather than from an average of the vertically integrated fluxes from the 17 individual soundings.

objectives that included documentation of the LLJ with dropsondes from above 500 mb, and 17 of these succeeded in placing a dropsonde in the LLJ.

Identification of the ideal locations for dropsondes to be released from the aircraft depended on a complex set of factors and was limited by the relatively minimal information on conditions below the aircraft that was available during a flight. Information onboard from the airborne tail and belly radars was useful, but it was the dropsonde data itself that provided the most reliable information from which to deduce in real time the position of the aircraft with respect to the relatively narrow LLJ beneath it. During CALJET, the value of visible, infrared, and water vapor satellite imagery, which was often 4 to 8 h old at the time an LLJ was encountered, was limited by the tendency for features in upper- and midlevel clouds to be poorly correlated with the presence of an LLJ. Partly because of these difficulties, a major effort created the capability to receive satellite data electronically via satellite on board the P-3. PACJET-01 was the first experiment to make use of this capability, although in a rather primitive form. It has since been improved and has become a standard of research aircraft operations.

b. Dropsonde data quality

The GPS dropsondes used here represented a major advance from past drospondes, which were limited in their vertical resolution and their ability to resolve the relatively shallow boundary layer. Without the relatively high vertical resolution (roughly 10 m) and low minimum altitudes (20 m) of the wind measurements, this paper would not be possible. The accuracy of the GPS dropsonde measurements are approximately 0.2°C for temperature, 5% for relative humidity (which is somewhat smaller than that described below for nearly saturated conditions), 0.5 m s^{-1} for the wind speed components, and 1.0 mb for pressure (Hock and Franklin 1999). Although some disruption in winds did occur because of electrification issues, and roughly 10% of the GPS dropsondes failed entirely, the data are largely of high quality.

However, a long-standing challenge for sounding systems is still a source of important measurement uncertainty in this study, that is, water vapor observations. Visual inspection of the 17 dropsonde profiles suggest that they possess a dry bias in the moist lower troposphere (i.e., constant offsets between temperature and dewpoint over a significant portion of a sounding), despite the fact that a recent comparative study between Vaisala dropsondes and rawinsondes indicate no significant humidity bias between these two similar instrumentation packages (Wang 2005). This is not surprising, given that the two sounding packages contain the same class of humidity sensors. Nevertheless, there are several known sources of humidity measurement error in rawinsondes (and, by extension, dropsondes). Most of the errors are temperature dependent at temperatures below ~−30°C (Miloshevich et al. 2001), which is considerably colder than what was observed in the layer

of interest beneath 500 mb by the subset of CALJET and PACJET-01 dropsondes used in this study. There is also a relative-humidity-dependent dry bias present at all temperatures with greater relative humidities yielding larger biases, as is reported in Wang et al. (2002) and Miloshevich et al. (2004). They also show a direct relationship between the age of the humidity sensor and the magnitude of the dry bias. These biases behave differently for different humidity sensor types, which have been changed periodically in the dropsondes throughout the years. The combined effects of these sources of error can result in underestimates of relative humidity as large as 10% for ambient relative humidities at ~90% (Wang et al. 2002; Miloshevich et al. 2004). Because the humidity sensor types and ages in some of the dropsondes released during CALJET and PACJET-01 are unknown, relative humidity corrections described in Wang et al. (2002) and Miloshevich et al. (2004) cannot be reasonably implemented. The implications of this dry bias are discussed in section 4.

c. Satellite and ground-based data

During CALJET, a pair of Geostationary Operational Environmental Satellites (*GOES-8* and *-9*) provided nearly continuous spatiotemporal observations over the Pacific and adjacent landmasses with their infrared, visible, and upper-tropospheric water vapor sensors. Two GOES satellites (*GOES-8* and *-10*) operated during PACJET-01. The GOES satellites also yielded 3-hourly measurements of tropospheric feature-tracked winds during CALJET (Velden et al. 1997; Nieman et al. 1997) and hourly measurements with much higher spatial coverage during the GOES Rapid-Scan Winds Experiment (GWINDEX) specifically designed for PACJET (Velden and Stettner 2001).

During both winter seasons, a ground-based suite of meteorological instruments designed to investigate orographic precipitation enhancement and precipitation microphysics was deployed in the coastal mountains near Cazadero (CZD; black dot in Fig. 1). This included a 915-MHz wind profiler (e.g., Carter et al. 1995), surface meteorological instruments, a vertically pointing S-band radar (White et al. 2000), and other sensors. Rain gauge data from CZD were used to determine the days when global reanalysis data were included in a set of composite synoptic-scale analyses (section 5b).

3. Dropsonde data analysis

a. Criteria for case selection

The pre-cold-frontal LLJ environment within landfalling extratropical cyclone warm sectors is a preferred region of large horizontal moisture flux (Ralph et al. 2004) and can produce heavy rainfall in steep coastal terrain because of enhanced orographic lifting of the moist air mass (Reynolds and Kuciauskas 1988; Heggli and Rauber 1988; Neiman et al. 2002; Ralph et al. 2003). It is believed that the heaviest orographic rains in midlatitude west coastal mountains occur within potentially unstable warm sectors devoid of significant large-scale lift, because the potential instability is preserved until acted upon by orographic lift (e.g., Lowndes 1968; Browning et al. 1974). Surprisingly, however, few examples of offshore pre-cold-frontal soundings have been presented in the literature to support this hypothesis. Therefore, to obtain mean thermodynamic profile characteristics in this key region of landfalling cyclones, the 196 and 88 dropsondes released during CALJET and PACJET-01, respectively, were examined for evidence of pre-cold-frontal LLJs. Because a focal point of the CALJET/PACJET observing strategy was to document the structure and physical processes in the LLJ region ahead of landfalling cold fronts over the eastern Pacific, a number of these dropsondes were released in or near the pre-cold-frontal LLJ environment (as described in section 2a). For the case selection process, an LLJ was defined as a maximum in total wind speed below 1.5 km MSL, residing beneath a local minimum aloft. This low-level maximum was required to be at least 2 m s^{-1} larger than the minimum aloft (as in Neiman et al. 2002). The determination that the sounding was positioned ahead of an advancing cold front was made using other dropsonde and airborne data (in situ and radar) from the same flight, as well as operational satellite data. At least one dropsonde released within each of 10 CALJET storms and 7 PACJET-01 storms met these criteria, although only one dropsonde was chosen from each storm so as to not emphasize one case over another (Fig. 1). For those storms with more than one applicable dropsonde, we chose the sounding with the largest IWV content to ensure that the sounding closest to the core of the atmospheric river was included.

A representative example of a dropsonde released into a pre-cold-frontal LLJ during CALJET is shown in Fig. 2, and a PACJET-01 example is provided in Fig. 3. These soundings and their 15 counterparts (not shown) exhibited the following common attributes: 1) released at or above 500 mb, 2) located within the comma-cloud tail of a landfalling extratropical cyclone, 3) small dewpoint depressions (i.e., nearly saturated conditions) below ~700 mb, 4) a warm-advection signature of clockwise turning of the wind direction with height below ~850 mb, 5) a southerly component flow at the surface and a westerly component aloft, and 6) an LLJ below 1.5 km MSL with relatively strong flow above 5 km MSL. The 17 soundings were combined into a composite or mean offshore sounding in an effort to portray conditions in the LLJ region ahead of a landfalling cold front. The mean latitude and longitude of these soundings is 34.06°N, 126.02°W, which is roughly 500 km offshore (southwest) of San Francisco, California (Fig. 1), and upstream of blocking effects.

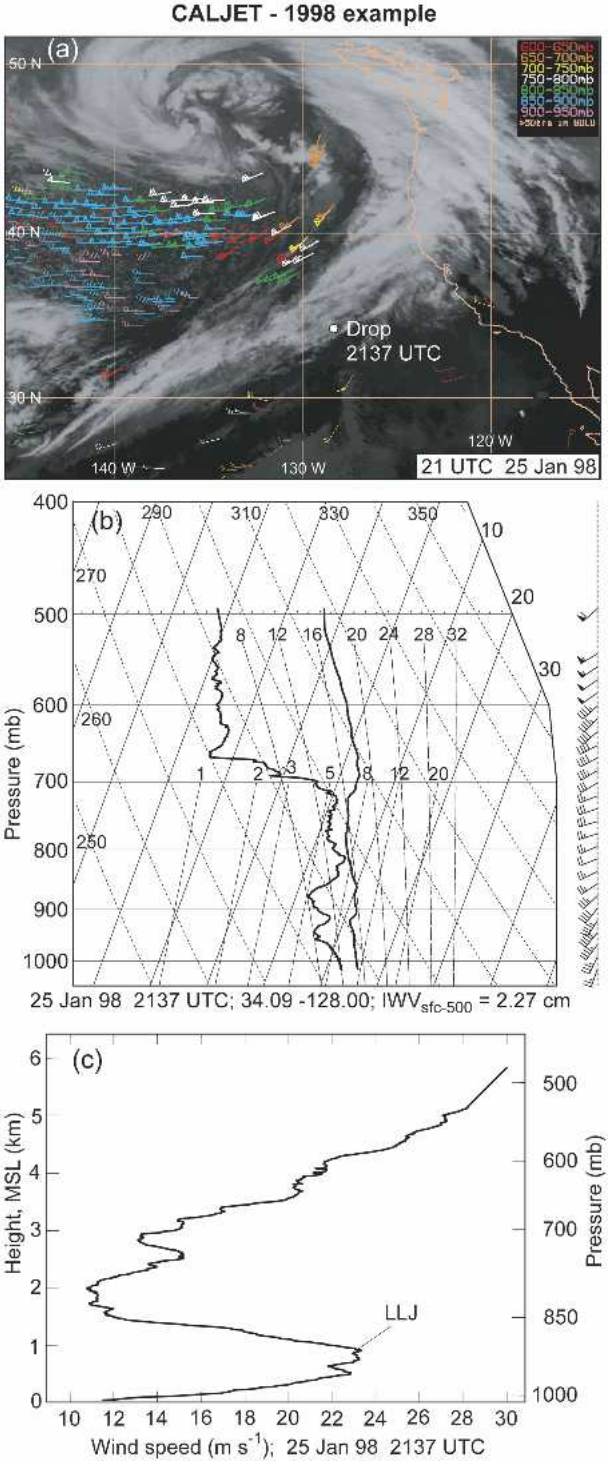

FIG. 2. (a) GOES infrared satellite image at 2100 UTC 25 Jan 1998, and the location of the pre-cold-frontal CALJET dropsonde released at 2137 UTC on the same day. Satellite-derived feature-tracked winds below 600 mb are shown (see inset key for pressure–altitude color coding). (b) Skew T—log$p$ sounding from the 2137 UTC dropsonde. Wind flags are 25 m s^{-1}, barbs are 5 m s^{-1}, and half barbs are 2.5 m s^{-1}. (c) Profile of wind speed (m s^{-1}) from the 2137 UTC dropsonde, with the LLJ marked.

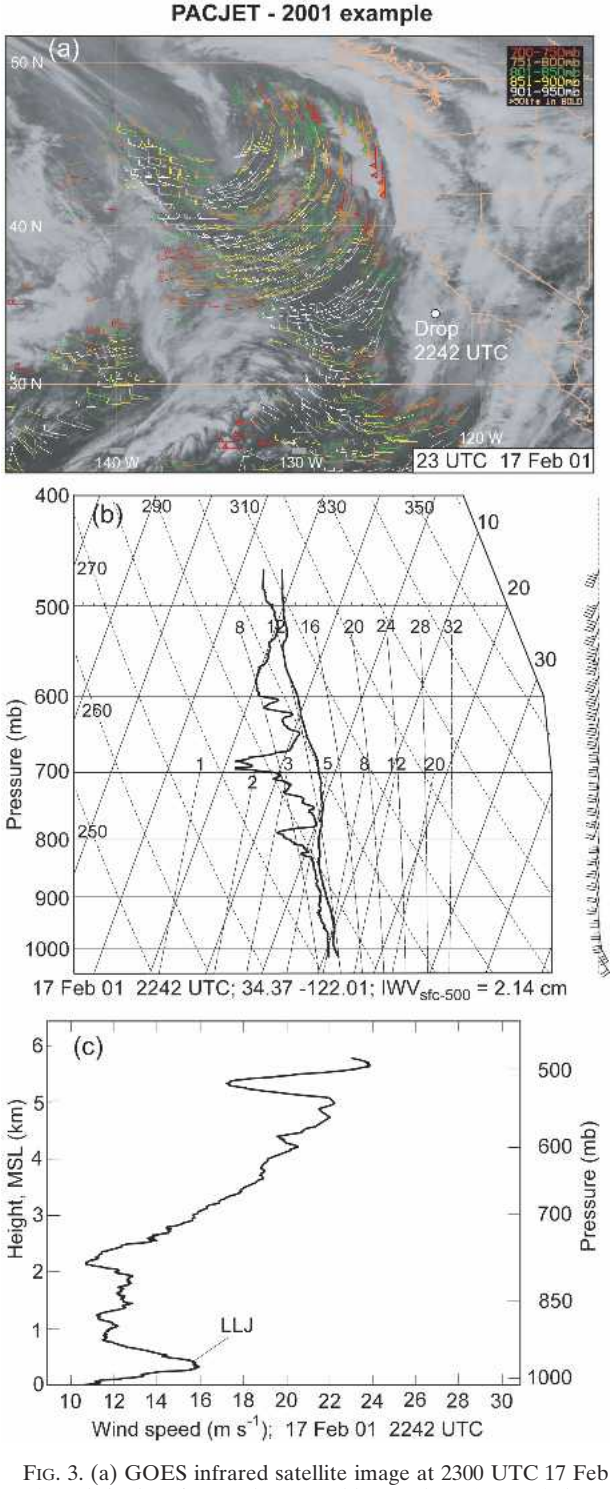

FIG. 3. (a) GOES infrared satellite image at 2300 UTC 17 Feb 2001, and the location of the pre-cold-frontal PACJET-01 dropsonde released at 2242 UTC on the same day. Satellite-derived feature-tracked winds below 700 mb are shown (see inset key for pressure–altitude color coding). (b) Skew T–log$p$ sounding from the 2242 UTC dropsonde. Wind flags and barbs are as in Fig. 2. (c) Profile of wind speed (m s^{-1}) from the 2242 UTC dropsonde, with the LLJ marked.

b. Methodology

To construct the composite sounding, the high-vertical-resolution (~10 m) thermodynamic and wind profiles recorded by each of the 17 dropsondes were interpolated onto a 100-m-resolution vertical grid. These gridded profiles were then averaged. Static stability was quantified from the composite profile by calculating a profile of the square of the Brunt–Väisälä frequency (henceforth BV frequency). Meridional and along-river moisture-flux profiles were also derived from the composite sounding. The methodology for constructing the BV and flux profiles is outlined below. The derived profiles presented in this paper were calculated from the composite sounding rather than from averaging the derived quantities from the individual soundings, because the focus here is on the smoother mean conditions rather than on the effects of small vertical-scale features that add noise to the derived profiles. Nevertheless, the latter approach yielded derived profiles (not shown) that were qualitatively similar to (albeit noisier than) those presented in sections 4 and 5.

1) BRUNT–VÄISÄLÄ CALCULATIONS

The BV frequency is commonly used to assess the static stability of atmospheric layers. In unsaturated air, the dry BV frequency can be determined using the relationship

$$N_d^2 = g(d\ln\theta/dz), \quad (1)$$

where $d\ln\theta/dz$ is the vertical gradient of the natural log of potential temperature, and $g = 9.8\ \mathrm{m\ s^{-2}}$ is the gravitational acceleration. The analog relationship for saturated conditions is calculated using the moist BV frequency of Durran and Klemp (1982):

$$N_m^2 = g\{[(1 + Lq_s/RT)/(1 + \varepsilon L^2 q_s/C_p RT^2)] \times [d\ln\theta/dz + (L/C_p T)dq_s/dz] - dq_w/dz\}, \quad (2)$$

where $L = 2.5 \times 10^6\ \mathrm{J\ kg^{-1}}$ is the latent heat of vaporization, $C_p = 1004.6\ \mathrm{J\ kg^{-1}\ K^{-1}}$ is the heat capacity for dry air at constant pressure, $R = 287\ \mathrm{J\ kg^{-1}\ K^{-1}}$ is the gas constant for dry air, $\varepsilon = 0.622$, T is the layer-mean sensible temperature, q_s is the layer-mean saturation water vapor mixing ratio, and q_w is the total-water (i.e., vapor + liquid) mixing ratio. Term 1 of Eq. (2) (everything except dq_w/dz) expresses the vertical gradient of equivalent potential temperature (θ_e), while term 2 (dq_w/dz) takes into account the vertical gradient of total-water mixing ratio, which Durran and Klemp (1982) show is reasonably approximated by the vertical gradient of saturation water vapor mixing ratio. Term 2 can be considered a second-order correction factor. It should be noted that this equation is a simplification of the full equation derived by Lalas and Einaudi (1974). Durran and Klemp (1982) present a quantitative comparison that demonstrates the suitability of this simplified equation, which is the basis for its use here.

We calculated profiles of dry and moist BV frequency from the composite sounding using the data from each adjacent pair of 100-m grid points. When calculating the moist BV frequencies, it was assumed that each layer of the composite sounding was cooled and moistened to the wet-bulb temperature via an isobaric process, such as might be caused by the evaporation of rainfall into the column. This process does not affect the first-order term 1 of Eq. (2) since θ_e is approximately conserved, but it can impact the second-order term 2 since the saturation water vapor mixing ratios are smaller following isobaric saturation. Since the stability depends critically on whether or not the air is saturated, it was essential to determine if the dry or moist BV value was more appropriate to consider within each layer of the composite sounding. This was achieved by determining the vertical displacement required for each 100-m layer to reach the lifting condensation level (LCL; Bolton 1980). Because the scale height of California's coastal mountains is 500–1500 m, one can consider that the air approaching the coast will be orographically lifted to saturation for vertical displacements smaller than that height range. Therefore, we conservatively assume that each 100-m layer requiring ≤ 400 m of lift to reach the LCL is saturated, and its stability will be given by N_m^2 rather than N_d^2. Note that this estimate of vertical displacement required to reach saturation is an overestimate due to the dry bias in the sonde data.

2) ESTIMATION OF HORIZONTAL MOISTURE FLUX

Ralph et al. (2004) extended the early findings of Browning and Pardoe (1973) that the pre-cold-frontal LLJ environment is a preferred region to observe elongated corridors of enhanced meridional moisture flux that Zhu and Newell (1998) refer to as atmospheric rivers, based on a dropsonde-intensive case study through a CALJET storm offshore of California and on a composite satellite data analysis over the eastern Pacific. The unique dropsonde dataset presented here offers the opportunity to build upon the Ralph et al. (2004) results by exploring the mean characteristics of the horizontal moisture flux in the LLJ region of 17 extratropical cyclones over the eastern Pacific during the CALJET and PACJET-01 winters.

The case selection criteria used in this paper focused on identifying sondes that sampled pre-cold-frontal conditions with an LLJ. Comparison of these cases with the criteria used by Ralph et al. (2004) to identify atmospheric rivers in Special Sensor Microwave Imager (SSM/I) integrated water vapor measurements confirmed that 13 of the 17 cases studied here roughly met the SSM/I criteria, two almost did so, one did not, and one could not be assessed. Thus, the drosponde data are used here to assess the vertical structure of atmospheric rivers. However, because the sondes may not have sampled the center of the region of maximum vertically integrated horizontal water vapor flux, the

magnitudes of the fluxes are an underestimate of the true maximum values of the flux within the rivers. The sonde from 25 January 1998 that met the pre-cold-frontal and LLJ criteria of this study (Table 1) illustrates this well because it was also used in the detailed analysis of an individual atmospheric river by Ralph et al. (2004) using 29 dropsondes in one case. This sonde was found to be located in the region of maximum horizontal water vapor transport in the layer below 800 mb, but it was 200 km southeast of the region of maximum IWV and vertically integrated horizontal water vapor flux (see Fig. 9 of Ralph et al. 2004). However, because it is only one case study, the representativeness of this 200-km offset to other cases remains uncertain.

The methodology employed to calculate the vertical profiles of horizontal moisture flux from each dropsonde and from the composite sounding is the same as in Ralph et al. (2004). Calculations are done both in terms of the meridional water vapor flux within the atmospheric-river environment, which Zhu and Newell (1998) found was responsible for >95% of the total meridional water vapor transport at midlatitudes, and in terms of the total "along river" flux that is most important for determining rainfall at the coast. The composite meridional and along-river moisture-flux profiles presented in this paper are derived from the composite sounding in Fig. 4. The composite along-river flux profiles require knowledge of the mean orientation of the along-river component of the flow, which was estimated by vector averaging the wind velocity at 1.0 km MSL from each sounding. The 1.0-km level corresponds to the altitude of the LLJ in the composite sounding, which, as will be shown later, is also roughly the central altitude of the layer responsible for 75% of the horizontal water vapor transport. The flux profiles are determined by layer averaging the dropsonde data into 50-mb increments between 1000 and 500 mb. The meridional, zonal, and along-river components of the flow within each 50-mb layer are then used to estimate the northward, eastward, and downriver advection of water vapor content in that layer. The flux calculations are assumed to be applicable in a 50-km window on either side of the dropsonde. The scale height of the meridional and along-river moisture-flux distribution for the composite sounding is quantified by calculating the cumulative fraction of the vertically integrated flux starting at the bottom of the sounding.

4. Composite dropsonde sounding results

The 17-case composite dropsonde sounding results are shown in Fig. 4. The skew T–log$p$ thermodynamic/wind-velocity diagram (Fig. 4a) portrays a nearly saturated atmosphere below ~800 mb (i.e., below ~2 km MSL) flowing in a direction approximately normal to the northwest–southeast-oriented California coastline. Clockwise turning of the wind with height in this layer is indicative of warm advection, consistent with conditions often found in a pre-cold-frontal LLJ environment (e.g., Browning and Pardoe 1973). Because the flow aloft at 600 mb (i.e., near the steering level) was from 230° and the associated cold fronts were typically moving toward the coast, the conditions captured by the composite sounding would, in a mean sense, ultimately impact California's coastal zone. The mean integrated water vapor (IWV) between the surface and 500 mb is 2.44 cm, with individual soundings as moist as 3.33 cm. These large values of IWV are typical of those found in narrow filaments of enhanced IWV associated with atmospheric rivers during the winter of 1997/98 over the northeastern Pacific Ocean (Ralph et al. 2004). However, the average peak value of IWV derived from SSM/I data in Ralph et al. (2004) was 2.81 cm, which is 15% greater than the mean of the 17 soundings used here. This difference may have arisen partly because the 17 soundings were chosen based on the presence of an LLJ, which, according to the case study in Ralph et al. (2004), is displaced to the warm side of the IWV maximum.

The composite wind speed profile (Fig. 4b) indicates the presence of a prominent (23.4 ± 9.4 m s^{-1}) LLJ at 1 km MSL, which has been shown to play a significant role in orographic rainfall enhancement in California's coastal mountains (Neiman et al. 2002; Ralph et al. 2003; Neiman et al. 2004). The altitude and magnitude of the composite LLJ core compare favorably with observations by Browning and Pardoe (1973) of six different LLJs in southwestern England, United Kingdom (their mean values were 27.5 m s^{-1} and 880 mb, respectively), even though only one of their LLJs was likely unaffected by orography. The companion composite profile of θ (Fig. 4c) exhibits a remarkably constant vertical gradient of approximately 4.5 K km^{-1} between the surface and 4 km MSL, which, in the absence of moisture effects, implies a very stable air mass. However, the effects of moisture are significant below 2 km MSL because the air in this layer is nearly saturated (Fig. 4f) and because θ_e decreases by ~1.5 K (Fig. 4d). The water vapor mixing ratio (Fig. 4e) decreases monotonically with height (1.7 g kg^{-1} km^{-1}) starting from a maximum value of 8.8 g kg^{-1} at the surface.

With the nearly saturated composite conditions below 2 km MSL (Fig. 4f), only 200–300 m of lift is required to reach the LCL (Fig. 5a), which is much smaller than the 500–1500-m height of the coastal mountains providing the orographic lift. The mean vertical displacement required to reach saturation in the lowest 2 km MSL is 266 m, but if the soundings are moistened by 5% (10%) at all altitudes to compensate for the dropsonde dry bias, the mean vertical displacement needed in this layer to reach saturation is only 164 m (67 m). The 400-m displacement threshold that is employed to determine the application of N_d^2 or N_m^2 in each 100-m layer of the composite BV profile (Fig. 5b) resides at 2.8 km MSL. Hence, the composite BV pro-

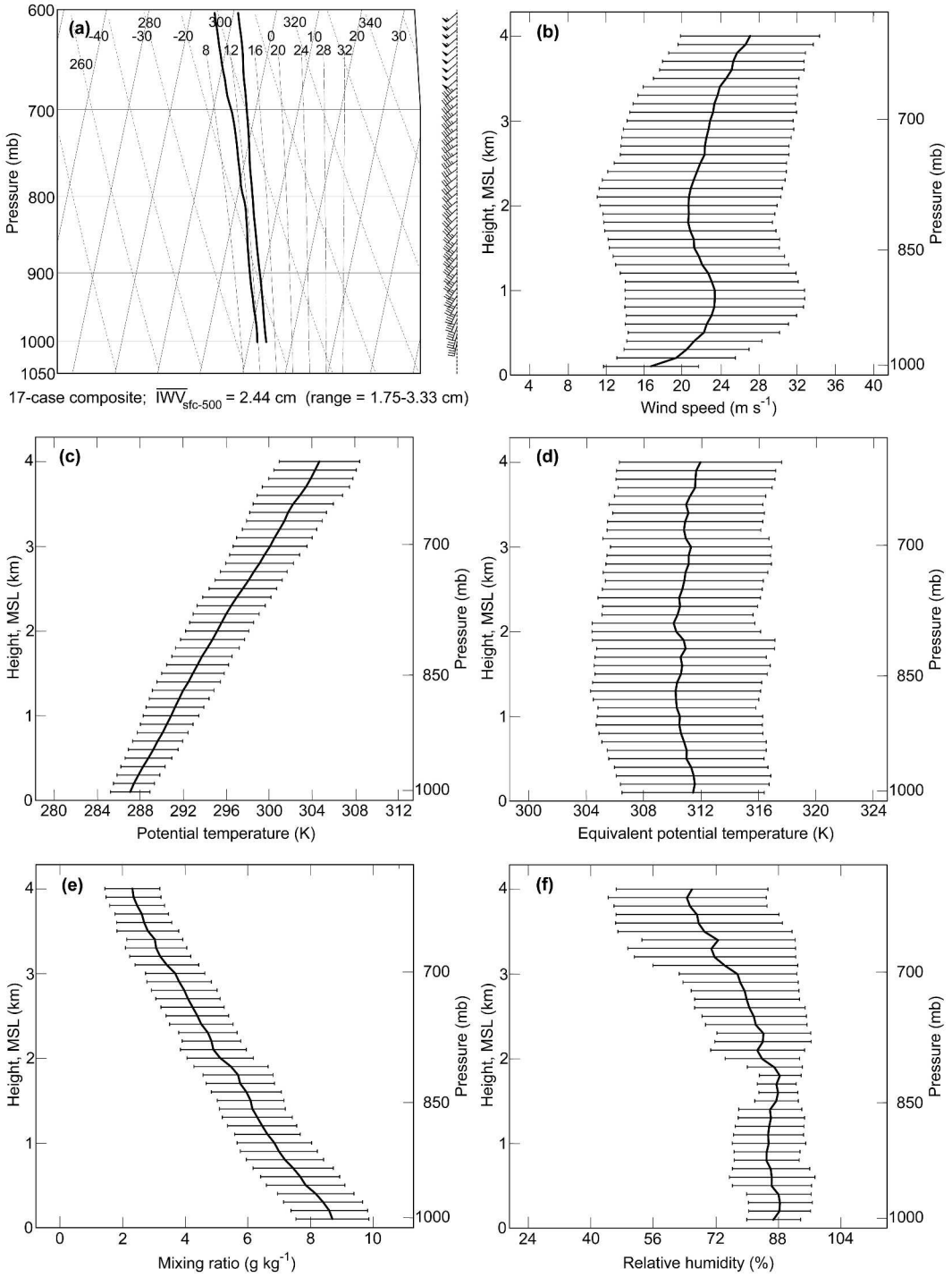

FIG. 4. Composite mean sounding (100-m vertical resolution) based on the 17 pre-cold-frontal dropsondes: (a) skew T–log$p$ portrayal (wind flags and barbs are as in Fig. 2), and profiles of (b) wind speed (m s^{-1}), (c) potential temperature (K), (d) equivalent potential temperature (K), (e) water vapor mixing ratio (g kg^{-1}), and (f) relative humidity (%). Standard deviation bars are shown in (b)–(f).

file comprises N_m^2 below this altitude and N_d^2 above. This composite profile shows that the air approaching the coastal mountains in the moisture-rich pre-cold-frontal LLJ environment is approximately neutrally stratified below 2.8 km. In addition, each of the 17 BV profiles that make up the composite possesses near-neutral conditions within at least part of this 2.8-km layer (not shown). Similar observations of nearly con-

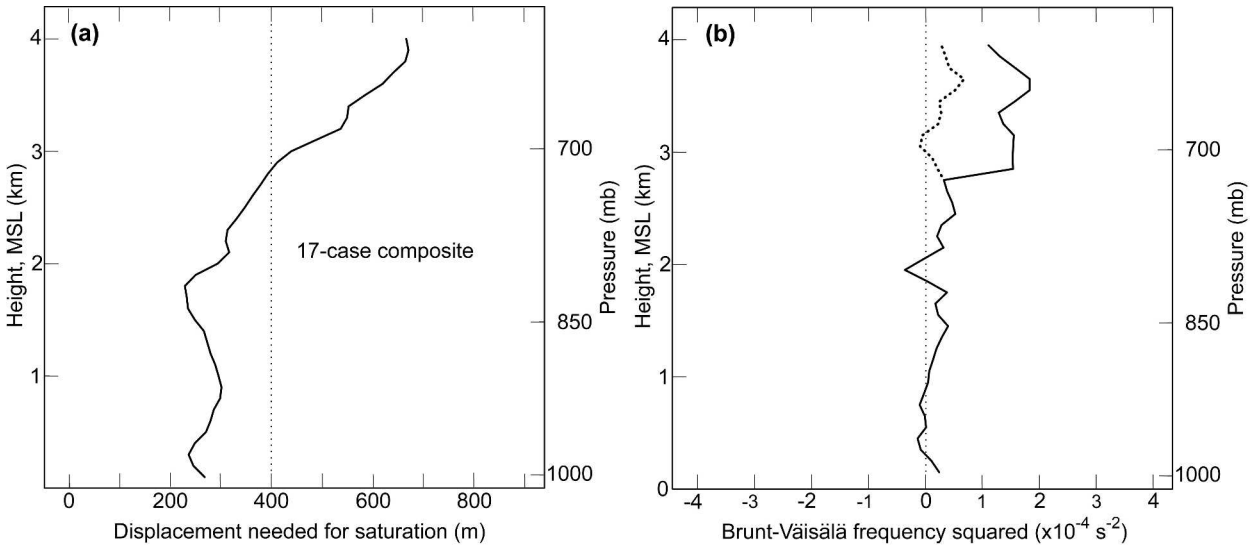

FIG. 5. Profiles of (a) the vertical displacement (m) required to saturate each level of the 17-case composite mean sounding, and (b) the square of the BV frequency ($\times 10^4$ s^{-2}) for each 100-m layer of the 17-case composite mean sounding. The moist (dry) BV frequency is used when less than (greater than) 400 m of displacement [dotted line in (a)] is required to achieve saturation. The dotted curve in (b) is a continuation of the moist BV profile from the altitude of the 400-m displacement threshold upward to 4 km MSL.

stant equivalent potential temperature with height in nearly saturated LLJ conditions were presented in Browning and Pardoe (1973), although calculations of the moist static stability [e.g., Eq. (2)] were not presented.

Given the documented dry bias of Väisälä dropsondes in moist conditions, the vertical displacement required to saturate the composite sounding (Fig. 5a) is overestimated. Hence, employment of the moist BV frequency likely extends deeper into the troposphere than 2.8 km MSL (see dotted line in Fig. 5b), which is already well above the scale height of California's coastal terrain. In addition, because the composite relative humidity profile is nearly constant in the lowest 2 km (Fig. 4f), the dry bias in this layer should be altitude independent. The age of individual dropsondes would also impact the humidity observations at different altitudes equally. Therefore, the dry bias and its relative humidity and age dependence should not significantly alter the vertical gradients of θ_e or water vapor mixing ratio, and therefore should not adversely affect the interpretation of the BV results within the shallow layer of the atmosphere (i.e., below ~2 km MSL) most directly impacted by orographically forced ascent.

These BV results add weight to the view (discussed in the introduction) that during periods of intense orographic precipitation, the atmosphere upwind of the orography is essentially neutral to vertical air-parcel displacements. From a theoretical point of view, one should expect an orographically modified flow consistent with neutral or nearly neutral conditions, that is, flow that will experience little or no resistance to lifting as it encounters the terrain [e.g., see numerical simulation results by Rotunno and Ferretti (2001) and Miglietta and Rotunno (2005)]. As discussed in those papers and references therein, although the case of neutral flow is the simplest, the possibility of a nonlinear switching between statically neutral and stable conditions from one location or time to another makes the problem extremely difficult. That this switching process is nonlinear can be appreciated by considering that the stability depends on air saturation, which depends on parcel displacement, which in turn depends on stability, and so on.

The impact of the observed composite conditions on the nature of orographically induced flows, described above, is a critical step in the process of transforming the horizontal water vapor transports, which are focused in atmospheric rivers, into precipitation on land. Not only do the composite sounding data provide insight into the nature of orographically induced flows, they also can help characterize the vertical structure of atmospheric rivers themselves, as described below.

Coarse-vertical-resolution [50 mb; this matches the resolution used in Ralph et al. (2004)] composite profiles of specific humidity (Fig. 6a) and the along-river and meridional wind speeds (Fig. 6b) reflect the observations shown in Figs. 4e and 4b (i.e., a steady decrease in moisture content with height and a low-level wind maximum associated with an LLJ). These observations were synthesized into vertical profiles of composite along-river and meridional moisture flux (Fig. 6c). The largest flux occurs in the lower troposphere where the largest moisture content coincides with the low-level wind maximum. Despite increasing along-river and me-

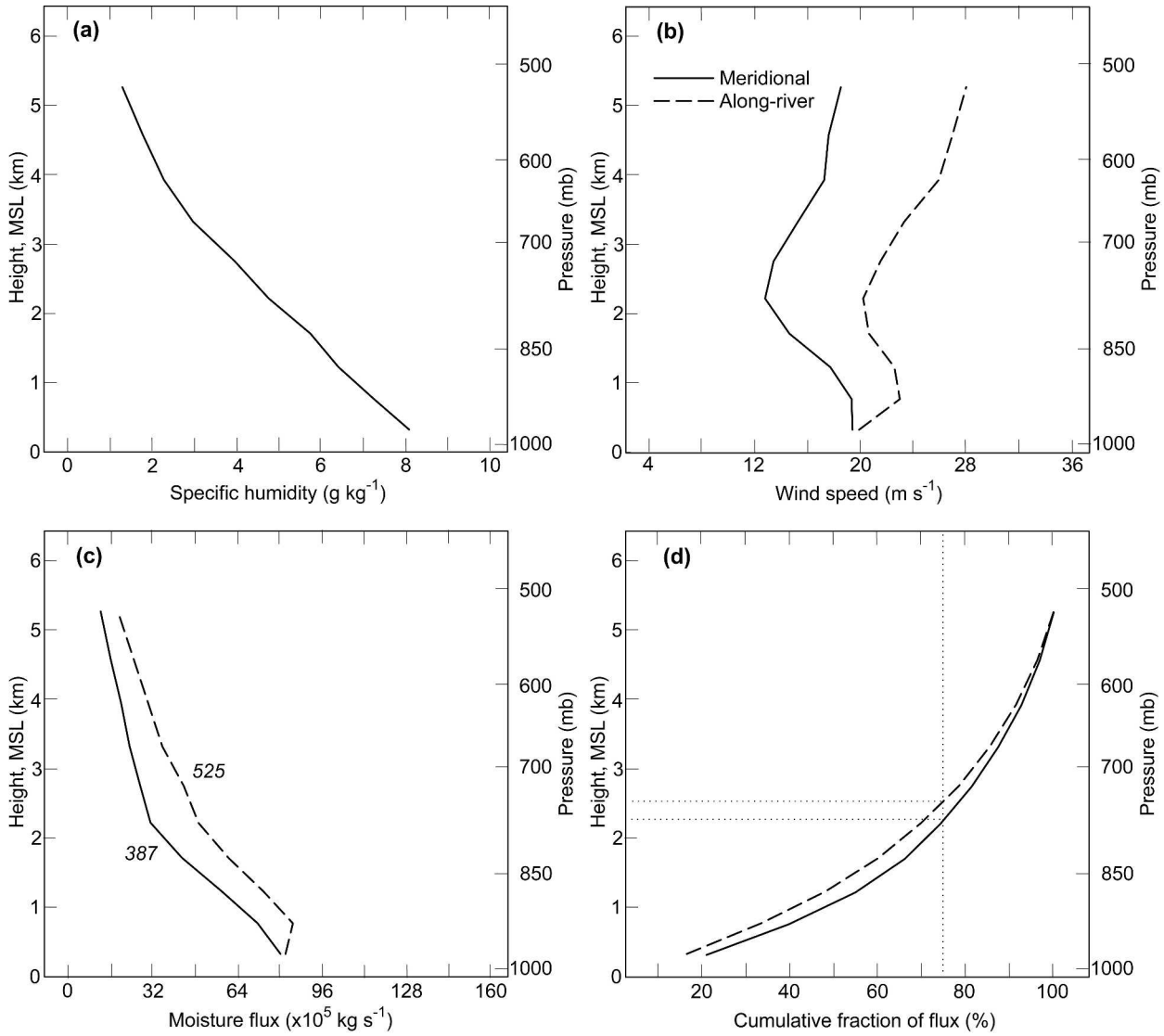

FIG. 6. Composite mean profiles (50-mb vertical resolution) based on the 17-case pre-cold-frontal sounding: (a) water vapor specific humidity (g kg^{-1}), (b) meridional and along-river wind speed (m s^{-1}), (c) meridional and along-river moisture flux ($\times 10^5$ kg s^{-1}), and (d) cumulative fraction (%) of meridional and along-river moisture flux. The 1000–500-mb moisture-flux values ($\times 10^5$ kg s^{-1}) are positioned next to the relevant curves in (c).

ridional flow with height above 2 km MSL, the fluxes decrease steadily aloft due to the decrease in moisture content with height. Consequently, 75% of the meridional (along river) moisture flux below 500 mb occurs in the lowest 2.25 km (2.50 km), as is apparent in the cumulative fractions shown in Fig. 6d. The composite along-river vertically integrated horizontal water vapor flux (525×10^5 kg s^{-1}) is 36% greater than the meridional component (Fig. 6c; Table 1) and 74% greater than the zonal component (Table 1). This detailed analysis of the horizontal moisture fluxes yields values that are comparable to the coarse estimates made by Browning and Pardoe (1973) using observations of LLJs in southwestern England, United Kingdom.[1] These results highlight the combined importance of the high moisture content and strong winds in the pre-cold-frontal LLJ environment to the efficient transport of moisture from the eastern Pacific into the coastal mountains. It also highlights the fact that coastal mountains oriented normal to the 216.7° mean orientation of the flow at 1 km in the atmospheric rivers (Table 1)

[1] Although it would have been desirable to duplicate the approach of Browning and Pardoe (1973) for calculating horizontal moisture fluxes, their approach was not described.

should be highly favored regions for orographic precipitation enhancement along the U.S. West Coast in the absence of blocking (e.g., Neiman et al. 2002). In the presence of blocking, a layer of enhanced static stability caps the shallow, terrain-trapped cold air and slopes downward to the surface immediately upstream of the mountains (e.g., Overland and Bond 1995; Doyle 1997), resulting in a terrain-induced baroclinic zone. The sloping isentropes within this zone represent a secondary orographic forcing mechanism for precipitation, thus producing rainfall enhancement upstream of the coastal orography (Doyle 1997; Neiman et al. 2002).

The detailed documentation of an atmospheric river in Ralph et al. (2004) indicates that the vertically integrated along-river horizontal water vapor flux at the position of the LLJ was 90% of the maximum value, which was found 200 km to its northwest. Thus, if the detailed case study is representative of most atmospheric rivers, then the maximum horizontal flux values found in the composites reported here underestimate the maximum values by about 10% due to their focus on the LLJ. In addition, the relative-humidity-dependent dry bias of the dropsondes could lead to a further underestimate by as much as 10%. Thus, the moisture-flux values derived from the 17 sondes represent lower-bound estimates by up to 20%. Finally, because the case study in Ralph et al. (2004) showed that the maximum vertically integrated water vapor fluxes were associated with a deeper layer of strong flux than that found in the LLJ region to its southeast, the scale height of the 75% cumulative fraction of flux determined here from the LLJ soundings is somewhat smaller than is likely to be found at the core.

5. Interannual variability

In an effort to assess the impact of short-term climate variability associated with the El Niño–Southern Oscillation (ENSO) on the static-stability and horizontal moisture-flux attributes in the pre-cold-frontal LLJ environment, the 17 soundings were partitioned into CALJET and PACJET-01 subsamples. The first step here is to briefly describe differences between the winters in terms of the phase of ENSO and the synoptic conditions associated with storms that affected the California coast. This is accomplished by developing composites that are based on the coarse (2.5° latitude × 2.5° longitude) daily global gridded dataset from the NCEP–NCAR reanalysis project (e.g., Kalnay et al. 1996). The second step is to diagnose differences and similarities found in the dropsonde data.

a. The phase of ENSO

Differences in the phase of ENSO between these winters were clearly evident in many variables over the Pacific basin, as is partly represented by the multivariate ENSO index (MEI) used to quantify the phase of ENSO (Wolter and Timlin 1993, 1998). The MEI was a near-record 2.72 during CALJET, thus signifying the presence of a strong warm-phase event commonly referred to as El Niño. The MEI during PACJET-01 was −0.58, revealing modest cold-phase or La Niña conditions. To further illustrate the differences, composite sea surface temperature (SST) analyses and anomalies[2] were constructed from the NCEP–NCAR reanalysis dataset for the 1998 CALJET and 2001 PACJET-01 winter seasons for the 3-month period January–March, and are shown in Fig. 7. The CALJET winter experienced anomalously warm SSTs in the equatorial eastern Pacific and along the west coast of North America, with anomaly values exceeding 2° to 3°C over large areas. In contrast, the PACJET-01 winter was characterized by modestly negative anomalies ranging from nearly 0°C to −1.5°C in these same areas.

b. Composite synoptic conditions in storms striking northern California

The large-scale conditions responsible for generating significant rainfall downstream of the dropsondes (i.e., in California's coastal zone) during these two disparate ENSO regimes were gauged by constructing composite synoptic-scale analyses using the NCEP–NCAR reanalysis dataset. For each significant daily rain event (i.e., ≥12.5 mm during a 0000–0000 UTC period) measured at the heavily instrumented coastal-mountain site at CZD during CALJET, NCEP–NCAR's daily gridded data for the day of the rain event were included in the composites. An analogous set of composites were generated for PACJET-01. A total of 33 and 17 events were used in the CALJET and PACJET-01 composites, respectively. Compared to using only those dates corresponding to the dropsonde data, this approach yielded 3 times the number of samples and overcame difficulties associated with adjusting for the differing locations of the dropsondes.

The mean storm characteristics responsible for significant rain events at CZD for the El Niño winter of 1998 (Figs. 8a–d) and the La Niña winter of 2001 (Figs. 8e–h) are strikingly different. For example, the composite 500-mb geopotential height analysis for CALJET exhibited low-latitude, quasi-zonal flow from the central Pacific to the west coast of California (Fig. 8a). Diffluent southwesterly flow aloft resided over CZD, immediately downstream of a broad short-wave trough axis. In contrast, 500-mb ridging over the eastern Pacific during PACJET-01 produced northwesterly flow downstream of the ridge and upstream of a sharp trough axis just offshore of California (Fig. 8e), although CZD was again beneath diffluent southwesterly

[2] The reanalysis anomaly for each year is obtained by subtracting the composite mean field from the long-term (1968–96) average for the 3-month date range.

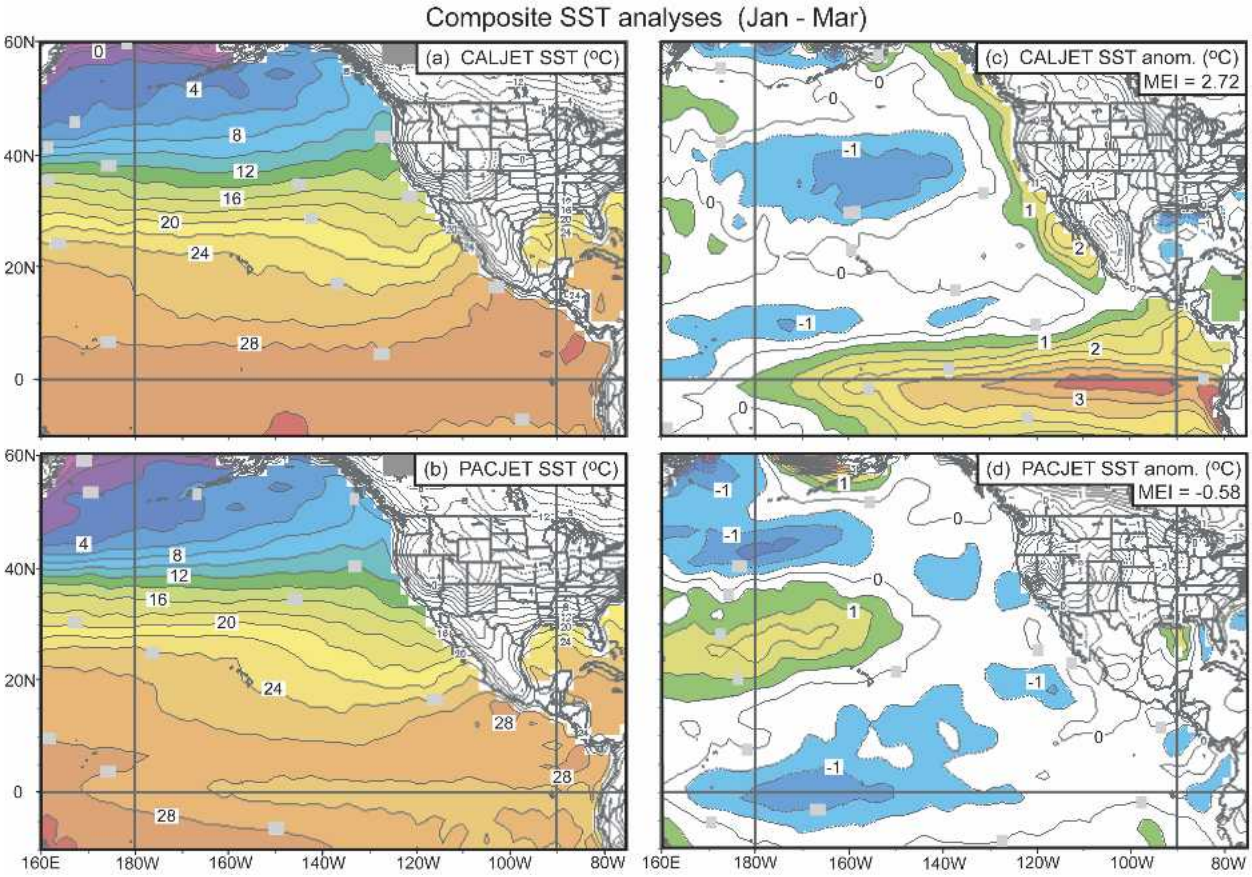

FIG. 7. Composite SST analyses (°C) for the 3-month Jan–Mar period derived from the NCEP–NCAR daily reanalysis global gridded dataset: SST means for (a) CALJET 1998 and (b) PACJET 2001, and SST anomalies for (c) CALJET 1998 and (d) PACJET 2001. The 3-month MEI values are shown in (c) and (d).

flow aloft. Companion geopotential height analyses at 925 mb also reveal significant differences (Figs. 8b, f). Namely, a broad low-level cyclone centered over the Gulf of Alaska during CALJET directed a lengthy west-southwesterly fetch from the relatively warm central Pacific into California, whereas a closed cyclone immediately offshore of the California–Oregon border during PACJET-01 resulted in a short southwesterly ocean fetch into California. Enhanced southerly component flow resided over CZD in both 925-mb meridional wind speed composites (Figs. 8c and 8g), although only the PACJET-01 composite showed northerly component flow offshore because of the presence of the closed cyclone circulation. A well-defined plume of large moisture content was directed at CZD in the CALJET IWV composite (Fig. 8d) but not in the corresponding PACJET-01 composite (Fig. 8h), thus revealing that the CALJET storms tapped into a richer supply of moisture than the PACJET-01 storms. And finally, the composite 925–700-mb layer-mean temperature at CZD (not shown) was 2.2°C versus −1.1°C for the CALJET versus PACJET-01 storms, respectively. The composite analyses suggest that the storms impacting the California coast during CALJET and PACJET-01 originated from different locations with different synoptic-scale airmass attributes.

To further define the synoptic conditions associated with significant rain events at CZD, mean low-level frontal positions were derived from distinct features in the composite 925-mb thermal and water vapor specific humidity fields (not shown). In the CALJET composites, a polar cold front extended northeastward from the open ocean to a southeast–northwest-oriented, coast-parallel occluded front that quite likely developed partly because of terrain effects (Bergeron 1937). East of the occlusion, the cold front aloft was situated north of CZD such that the mean conditions responsible for significant rainfall at CZD were tied to the pre-cold-frontal environment. Significant rain events at CZD also occurred, on average, in the pre-cold-frontal regime during PACJET-01. During both winters, the mean cold frontal passage offshore was preceded by an IWV plume and enhanced southerly component flow commonly found in atmospheric rivers (Ralph et al.

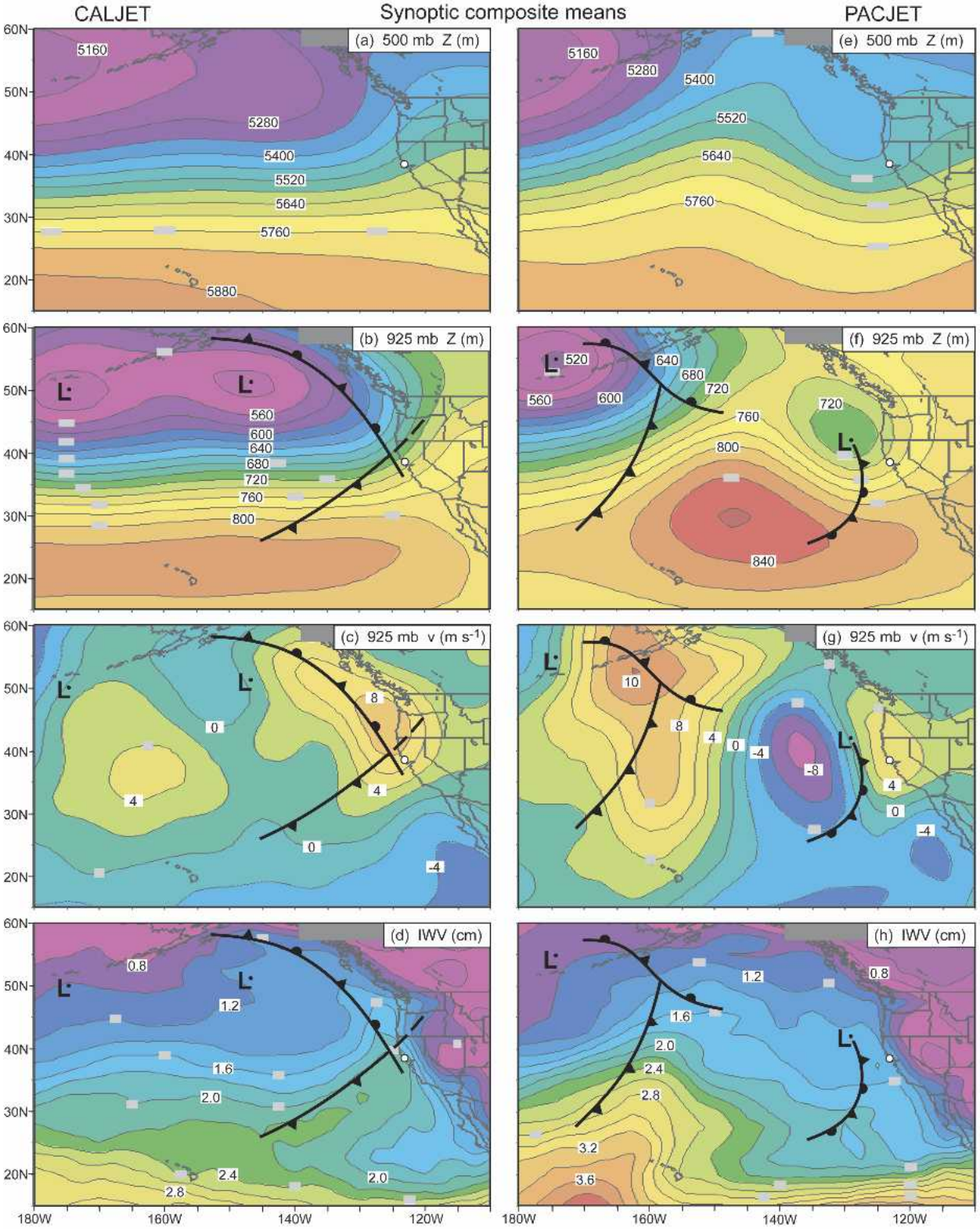

FIG. 8. Composite synoptic-scale mean analyses derived from the NCEP–NCAR daily reanalysis global gridded dataset for daily rain events (i.e., from 0000–0000 UTC) at CZD (bold white dot) exceeding 12.5 mm during (a)–(d) CALJET 1998 and (e)–(h) PACJET 2001: (a),(e) 500-mb geopotential height (m); (b),(f) 925-mb geopotential height (m); (c),(g) 925-mb meridional wind speed (m s^{-1}); and (d),(h) integrated water vapor (cm). Standard frontal notation is used to mark the composite frontal positions.

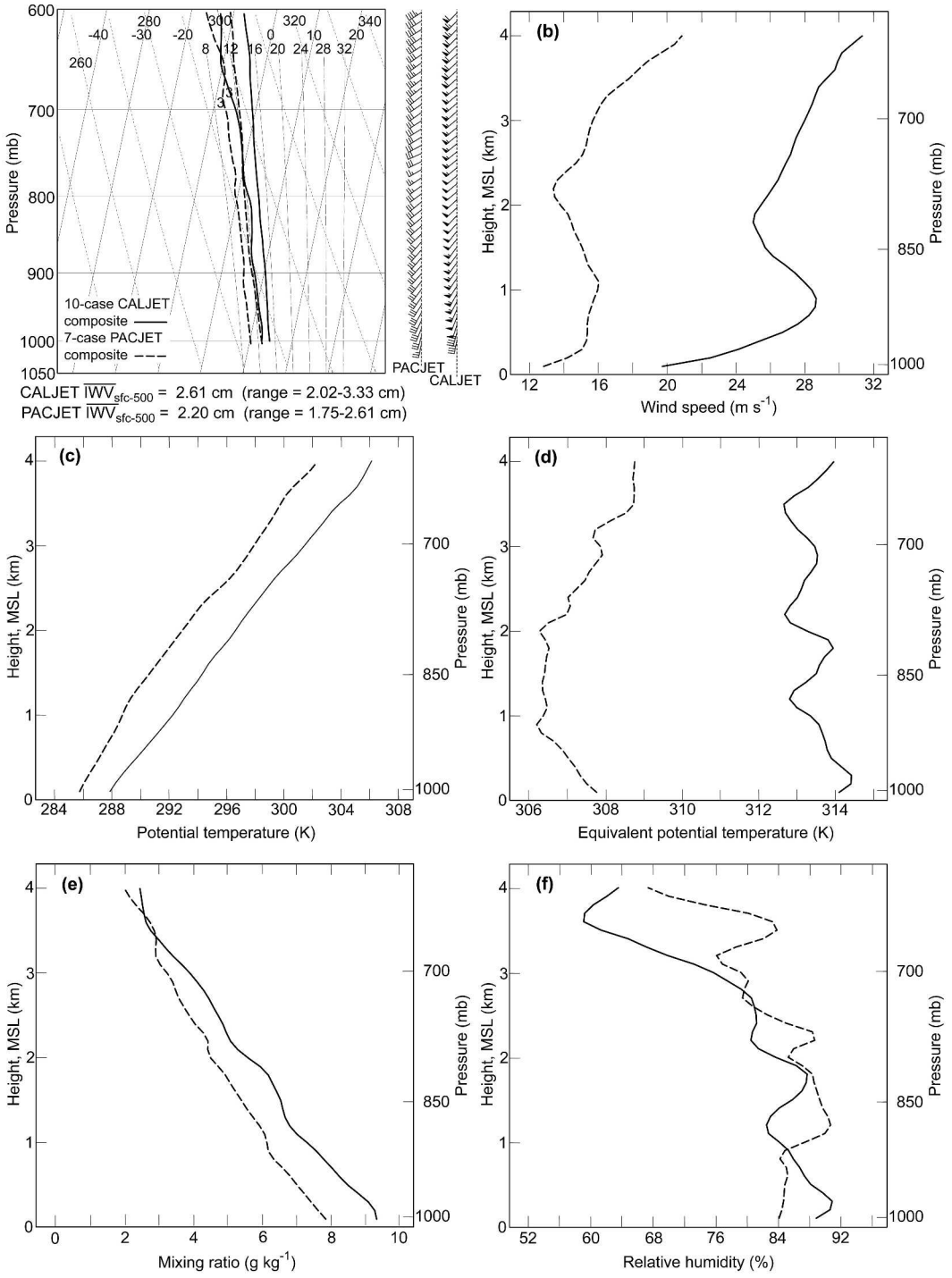

FIG. 9. The same as in Fig. 4, except for the composite mean profiles calculated from the 10 CALJET pre-cold-frontal dropsondes (solid curves) and 7 PACJET-01 pre-cold-frontal dropsondes (dashed curves).

2004), although the IWV plume was much more pronounced during CALJET than PACJET-01. (The primary IWV plume and meridional flow during PACJET-01 coincided with a cold front extending southward from an occluded cyclone over the Aleutians.) Hence, CZD was located in approximately the same storm-relative position as the 17 dropsondes released over the eastern Pacific.

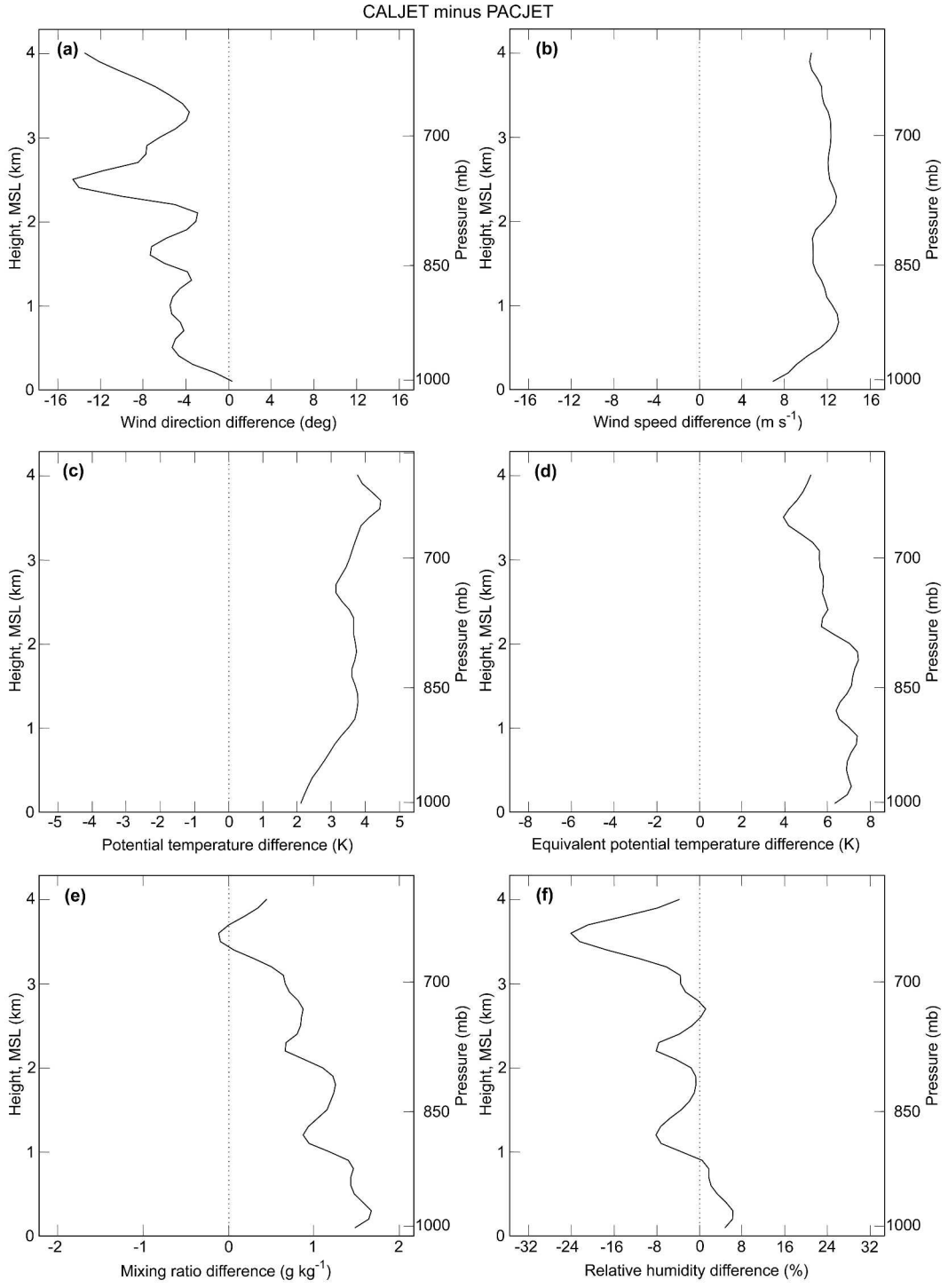

FIG. 10. Vertical profiles of the difference between the composite mean CALJET and PACJET profiles shown in Fig. 9.

c. Composite sounding comparisons

The 10-case and 7-case CALJET and PACJET-01 composite soundings are shown side-by-side in Fig. 9, and their differences are presented in Fig. 10. Additional key attributes of each sounding and of each season are shown in Table 1. The skew *T*–log*p* panel (Fig. 9a) highlights the similarity in the nearly saturated conditions below ~2 km MSL (see also Figs. 9f and 10f), the low-level onshore flow directed nearly orthogonal

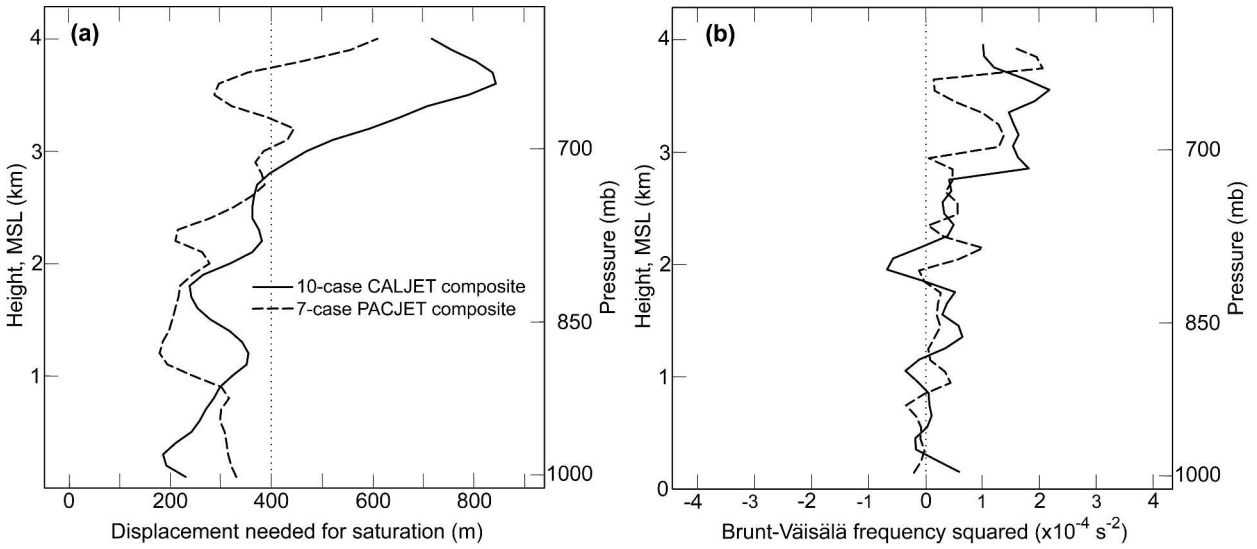

FIG. 11. The same as in Fig. 5, except for the composite mean profiles calculated from the 10 CALJET pre-cold-frontal dropsondes (solid curves) and 7 PACJET-01 pre-cold-frontal dropsondes (dashed curves).

to California's coastal mountains, the warm-advection veering with height below ~2 km MSL, and the height of the LLJ at ~1 km MSL (see also Fig. 9b). Nevertheless, fundamental differences are also observed that are fully consistent with the stark differences between the CALJET and PACJET-01 synoptic composites (e.g., Fig. 8). For example, the mean 1000–500-mb IWV content in the pre-cold-frontal LLJ environment is 19% larger during CALJET than PACJET-01 (2.61 versus 2.20 cm, respectively), which reflects the offset in the water vapor mixing-ratio profiles below 4 km MSL (Figs. 9e and 10e). In fact, the mean IWV value during CALJET matches the largest value observed during PACJET-01. The mean pre-cold-frontal LLJ magnitude is considerably larger during CALJET than PACJET-01 (28.5 versus 15.9 m s^{-1}, respectively; Figs. 9b and 10b). In addition, the flow is more meridional during CALJET (Fig. 10a), which is consistent with the observation that storm circulations during developed El Niño episodes tend to be more meridional than those during non–El Niño episodes (e.g., Rasmusson and Wallace 1983; Webb and Betancourt 1992). Sensible heat content is uniformly 2–4-K warmer below 4 km MSL during CALJET (Figs. 9c and 10c), resulting in a freezing level that is 527 m higher. The combined effects of enhanced heat and moisture yield a CALJET θ_e profile that is 5–8-K warmer than its PACJET-01 analog (Figs. 9d and 10d). The comparative profiles reveal that the CALJET storms, which coincided with a near-record El Niño episode, were stronger, warmer, and more moist than their PACJET-01 counterparts. This result is consistent with the fact that the polar and subtropical jet streams are often displaced southward and eastward during El Niño conditions (e.g., Rasmusson 1985; Cayan and Webb 1992; Livezey et al. 1997), resulting in an anomalously strong and active southern storm track into southern California.

Despite the fundamentally different ENSO-modulated thermodynamic and kinematic characteristics found in the CALJET and PACJET-01 storms, the impact of these modulations on the mean static stability in the pre-cold-frontal LLJ air masses approaching the coast is minimal (Fig. 11). Namely, the 400-m vertical displacement threshold resides at similar altitudes (2.8–3.0 km) for the mean CALJET and PACJET-01 air masses, below which less than 400 m of lift is required by the coastal terrain for these air masses to reach saturation. Consequently, the CALJET and PACJET-01 BV profiles are each composed of N_m^2 beneath this threshold altitude, and both BV profiles show approximately neutral low-level stratification with respect to saturated conditions. Hence, conditions are conducive to orographic precipitation enhancement when pre-cold-frontal LLJ air masses impact the coastal mountains, regardless of the phase of ENSO. Rainfall observations between the coastal mountain site at CZD and a nearby coastal site at Bodega Bay (BBY; 35 km south of CZD) during CALJET and PACJET-01 support this assertion. For the period 1 January–7 March (i.e., the 9-week period when rainfall measurements were taken at both sites during both experiments), the average rainfall at CZD was more than twice that at BBY (i.e., the CZD/BBY rainfall ratios were 2.19:1 and 2.01:1 during CALJET and PACJET-01, respectively). The larger CALJET ratio may reflect the fact that greater low-level water vapor content and stronger low-level winds were directed at the coast during CALJET than PACJET-01 (Figs. 9e and 9b), but it appears that the difference in ratios cannot be attributed to significant differences in static stability below 3 km MSL. These

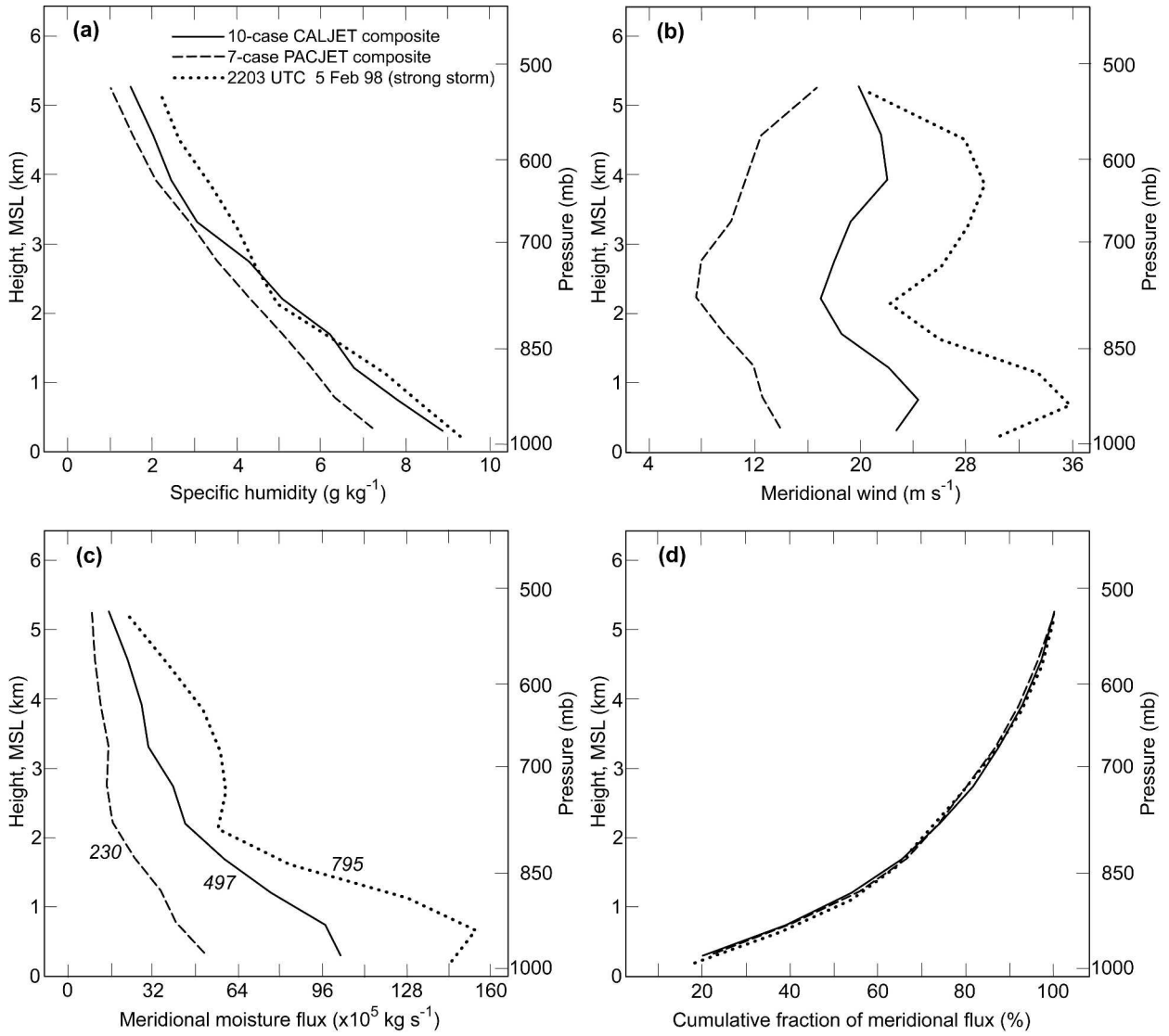

FIG. 12. The same as in Fig. 6, except for the composite mean profiles calculated from the 10 CALJET pre-cold-frontal dropsondes (solid curves) and 7 PACJET-01 pre-cold-frontal dropsondes (dashed curves) using meridional wind speed only. Profiles from a pre-cold-frontal dropsonde released within a strong storm on 5 Feb 1998 are also shown (dotted curves).

results are consistent with those of Ralph et al. (2003), who show a direct connection between greater low-level moisture content/onshore flow in the central California coastal mountains during El Niño winters than non–El Niño winters and larger annual peak flooding episodes (which arise largely because of orographic precipitation enhancement) in the same region during El Niño winters.

Differences between the two winters in terms of meridional water vapor fluxes are shown in Fig. 12.[3] The dropsondes recorded greater moisture content and stronger meridional flow during CALJET than PACJET-01 (Figs. 12a and 12b), which led to much stronger meridional moisture fluxes in the CALJET composite (Fig. 12c). Throughout the entire depth of the atmosphere below 500 mb, the mean flux is larger during CALJET than PACJET-01, such that the total 1000–500-mb flux is more than twice as large during CALJET (497×10^5 versus 230×10^5 kg s^{-1}; Table 1). This result suggests that the northward transport of moisture toward California's coastal mountains is larger during El Niño winters and, therefore, may also contribute to greater orographic precipitation enhancement during the warm phase of ENSO. Because individual strong storms, such as that observed on 5 February 1998 dur-

[3] Because the differences between meridional and along-river fluxes in these annual composites are very similar to those shown in the 2-yr composites presented in Fig. 6, the along-river fluxes for each year are not shown here.

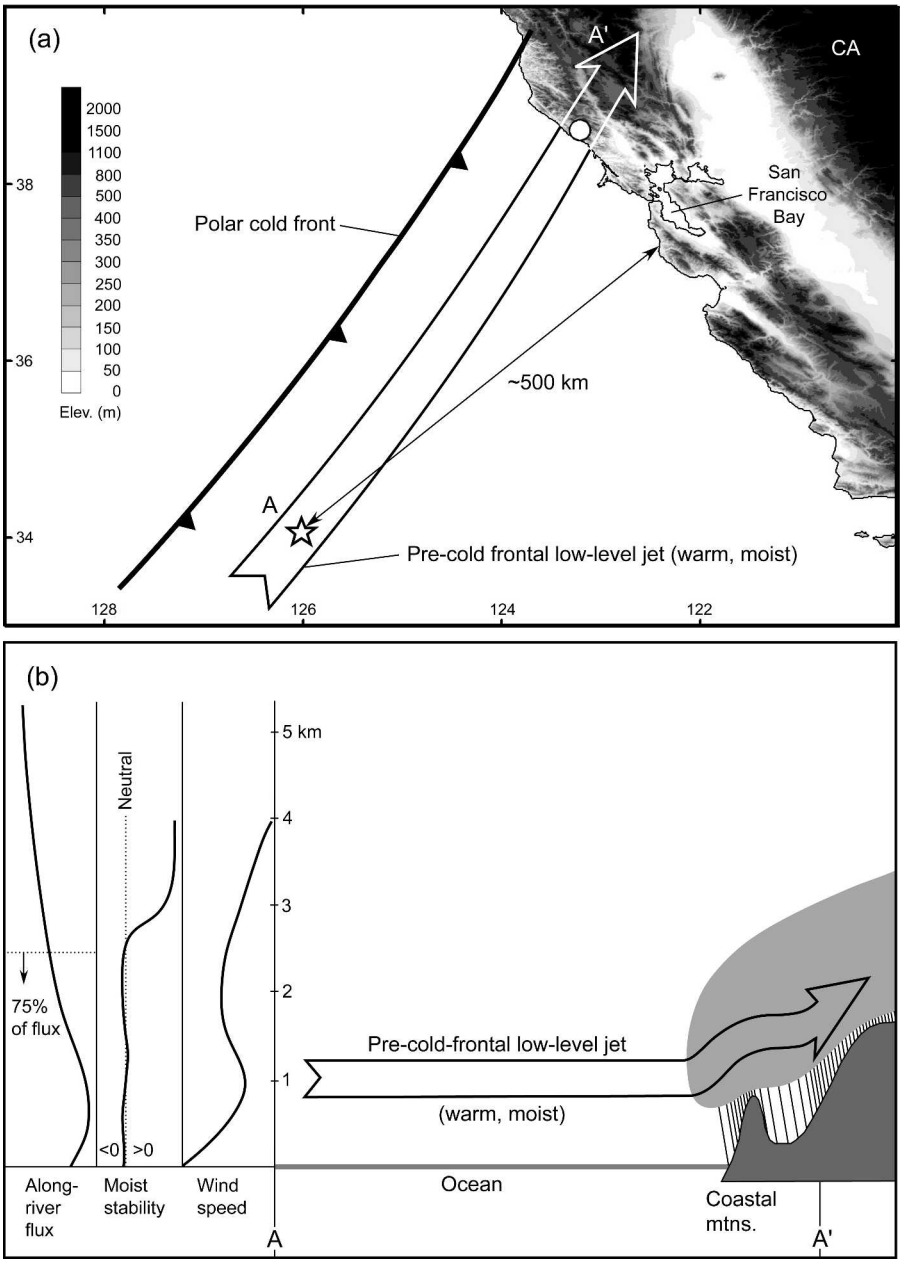

FIG. 13. Conceptual representation focusing on conditions in the pre-cold-frontal LLJ region of a landfalling extratropical cyclone over the northeastern Pacific Ocean. (a) Plan-view schematic showing the relative positions of an LLJ and trailing polar cold front. The average position of the 17 dropsondes used in this study is shown with a star (~500 km offshore of San Francisco), and the Cazadero microphysics site is marked with a bold white dot. The points A and A′ along the LLJ provide the approximate endpoints for the cross section in (b). (b) Cross section schematic along the pre-cold-frontal LLJ [i.e., along A–A′ in (a)] highlighting the offshore vertical structure of wind speed, moist static stability, and along-river moisture flux at the location of the altitude scale. Schematic orographic clouds and precipitation are shown, with the spacing between the rain streaks proportional to rain intensity.

ing CALJET, can possess even greater moisture content and stronger winds, the corresponding meridional moisture flux in these storms can be quite large (e.g., see Figs. 12a–c). Remarkably, despite the fundamental difference in the meridional flux magnitudes between CALJET, PACJET-01, and an individual strong storm, the scale height within which the meridional water vapor fluxes is concentrated is nearly identical (Fig. 12d);

that is, 75% of the meridional moisture transport is confined to the lower troposphere below 2.26 ± 0.03 km MSL. It should be noted that the storm-total rainfall at a given location depends also upon the duration of the storm. Analysis of this important dimension of the problem will be addressed in future work.

6. Conclusions

The observational dropsonde analyses presented here provide unique documentation of the conditions in the pre-cold-frontal environment of extratropical cyclones over the northeastern Pacific Ocean, including strong winds in an LLJ, large water vapor content, and neutral stratification with respect to moist ascent. These attributes combine to create strong horizontal water vapor fluxes as part of atmospheric rivers that are responsible for almost all of the meridional water vapor transport at midlatitudes (Zhu and Newell 1998; Ralph et al. 2004). When this potent portion of a storm strikes coastal mountains, the neutral stratification, strong horizontal wind, and high water vapor content lead to heavy orographic precipitation (e.g., Rotunno and Ferretti 2001). While these concepts have been long understood, the contribution of this paper is to provide unique quantitative descriptions of the mean offshore conditions found in this region of landfalling extratropical cyclones that is so important to both quantitative precipitation and flood forecasting as well as to the global water cycle. Figure 13 summarizes the results schematically, including quantitative information on mean aspects of the vertical profiles of wind speed, stratification, and horizontal water vapor transport far upstream of orographic influences. Specifically, a layer of moist neutral stability extends upward from the sea surface to well above the altitude of the pre-cold-frontal LLJ and California's coastal mountains, and the moist neutrality also coincides with the layer above the sea surface where 75% of the along-river flux is contained. These overlapping sets of conditions are highly conducive to orographic precipitation enhancement in the coastal mountains.

It is not uncommon for a coastal mountain site in California to receive 100–200 mm of rain in 24–36 h when struck by one of these features (e.g., Neiman et al. 2002, 2004; Ralph et al. 2003). These precipitation maxima can be very localized as a result of orographically forced ascent and descent. This spatial variability on local scales can influence flooding (e.g., Ralph et al. 2003), for which improved prediction requires understanding of the orographically induced airflow perturbations. Because the stratification is neutral with respect to saturated conditions, but is quite stable with respect to unsaturated conditions, the detailed structure and evolution of the orographic response can switch rapidly from one regime to another (Miglietta and Rotunno 2005).

The availability of data from two very different winter seasons revealed that several attributes of the storms varied significantly from the strong El Niño winter of 1998 (CALJET) to those from the modest La Niña winter of 2001 (PACJET-01). In particular, 2001 was characterized by 44% weaker winds in the LLJ, 10%–20% less water vapor content, 3°–4°C colder potential temperature, and >50% less horizontal water vapor flux. However, two key attributes did not vary significantly. The scale height of the horizontal water vapor fluxes in atmospheric rivers did not vary with ENSO, despite major differences in the storm track, and moist neutral conditions in the pre-cold-frontal LLJ were present in both winter-season composites and extended to 2.8–3.0 km MSL, which is well above the height of the coastal mountains.

The composite kinematic and thermodynamic characteristics presented here can be used for a variety of future analyses, including theoretical studies of orographic precipitation, evaluation of numerical model performance, and assessment of what types of observations are needed offshore to improve QPF and flood forecasting. An important implication of the moist neutrality below ~3 km is that the flow should readily ascend the relatively shallow coastal ranges without inducing blocking. However, the fact that blocking is commonly observed (e.g., Neiman et al. 2002, 2004) indicates that an alternative process must be active, for example, offshore advection of cool continental air through gaps in the coast ranges. Finally, more numerous and detailed observations of the cross-river structure are needed to better understand the relationship between the core of atmospheric rivers and the position of the LLJ, as well as the correlation between the maximum value of IWV in atmospheric rivers (which SSM/I satellite data provide) and the total along-river water vapor flux.

Acknowledgments. This paper would not have been possible without the talented and dedicated efforts of all the scientists, flight crews, and other CALJET/PACJET participants who contributed to the experiments, particularly those from NOAA's Aircraft Operations Center, Environmental Technology Laboratory, National Severe Storms Laboratory, Forecast Systems Laboratory, National Weather Service, the Naval Postgraduate School, and the Desert Research Institute. Dr. Larry Miloshevich provided invaluable assistance in understanding the dropsonde humidity sensor errors, while Dr. Gary Wick contributed through assistance in examining SSM/I satellite data for evaluation of atmospheric-river conditions. Figures were expertly prepared by Jim Adams and Dr. Allen White. We appreciate the thoughtful input from Keith Browning and two additional anonymous reviewers. Their efforts improved the scope and quality of this manuscript.

REFERENCES

Andrews, E. D., R. C. Antweiler, P. J. Neiman, and F. M. Ralph, 2004: Influence of ENSO on flood frequency along the California coast. *J. Climate,* **17,** 337–348.

Bergeron, T., 1937: On the physics of fronts. *Bull. Amer. Meteor. Soc.,* **18,** 265–275.

——, 1965: On the low-level redistribution of atmospheric water caused by orography. *Proc. Int. Conf. on Cloud Physics*, Tokyo, Japan, IAMAP/WMO, 96–100.

Bjerknes, J., and H. Solberg, 1921: Meteorological conditions for the formation of rain. *Geofys. Publ.,* **2,** 1–60.

Bolton, D., 1980: The computation of equivalent potential temperature. *Mon. Wea. Rev.,* **108,** 1046–1053.

Browning, K. A., 1980: Structure, mechanism, and prediction of orographically enhanced rain in Britain. *Orographic Effects in Planetary Flows,* R. Hide and P. W. White, Eds., GARP Publication Series, No. 23, World Meteorological Organization, 85–114.

——, and C. W. Pardoe, 1973: Structure of low-level jet streams ahead of mid-latitude cold fronts. *Quart. J. Roy. Meteor. Soc.,* **99,** 619–638.

——, F. F. Hill, and C. W. Pardoe, 1974: Structure and mechanism of precipitation and the effect of orography in a wintertime warm sector. *Quart. J. Roy. Meteor. Soc.,* **100,** 309–330.

Carter, D. A., K. S. Gage, W. L. Ecklund, W. M. Angevine, P. E. Johnston, A. C. Riddle, J. S. Wilson, and C. R. Williams, 1995: Developments in UHF lower tropospheric wind profiling at NOAA's Aeronomy Laboratory. *Radio Sci.,* **30,** 997–1001.

Cayan, D. T., and R. H. Webb, 1992: El Niño/Southern Oscillation and streamflow in the western United States. *Historical and Paleoclimate Aspects of the Southern Oscillation*, H. F. Diaz and V. Markgraf, Eds., Cambridge University Press, 29–68.

Colle, B. A., 2004: Sensitivity of orographic precipitation to changing ambient conditions and terrain geometries: An idealized modeling perspective. *J. Atmos. Sci.,* **61,** 588–606.

Douglas, C. K. M., and J. Glasspoole, 1947: Meteorological conditions in orographic rainfall in the British Isles. *Quart. J. Roy. Meteor. Soc.,* **73,** 11–38.

Doyle, J. D., 1997: The influence of mesoscale orography on a coastal jet and rainband. *Mon. Wea. Rev.,* **125,** 1465–1488.

Durran, D. R., and J. B. Klemp, 1982: On the effects of moisture on the Brunt–Väisälä frequency. *J. Atmos. Sci.,* **39,** 2152–2158.

Heggli, M. F., and R. M. Rauber, 1988: The characteristics and evolution of supercooled water in wintertime storms over the Sierra Nevada: A summary of microwave radiometric measurements taken during the Sierra Cooperative Pilot Project. *J. Appl. Meteor.,* **27,** 989–1015.

Hock, T. F., and J. L. Franklin, 1999: The NCAR GPS dropsonde. *Bull. Amer. Meteor. Soc.,* **80,** 407–420.

Jorgensen, D. P., and B. F. Smull, 1993: Mesovortex circulations seen by airborne Doppler radar within a bow-echo mesoscale convective system. *Bull. Amer. Meteor. Soc.,* **74,** 2146–2157.

——, T. Matejka, and J. D. DuGranrut, 1996: Multi-beam techniques for deriving wind fields from airborne Doppler radars. *J. Meteor. Atmos. Phys.,* **59,** 83–104.

Kalnay, E., and Coauthors, 1996: The NCEP/NCAR 40-Year Reanalysis Project. *Bull. Amer. Meteor. Soc.,* **77,** 437–471.

Lalas, D. P., and F. Einaudi, 1974: On the correct use of the wet adiabatic lapse rate in stability criteria of a saturated atmosphere. *J. Appl. Meteor.,* **13,** 318–324.

Langland, R. H., and Coauthors, 1999: The North Pacific Experiment (NORPEX-98): Targeted observations for improved North American weather forecasts. *Bull. Amer. Meteor. Soc.,* **80,** 1363–1384.

Livezey, R. E., M. Masutani, A. Leetma, H. Rui, M. Ji, and A. Kumar, 1997: Teleconnective response of the Pacific–North American region atmosphere to large central equatorial Pacific SST anomalies. *J. Climate,* **10,** 1787–1820.

Lowndes, S., 1968: Forecasting large 24-h rainfall totals in the Dee and Clwyd River Authority Area from September to February. *Meteor. Mag.,* **97,** 226–235.

Miglietta, M. M., and R. Rotunno, 2005: Simulations of moist nearly neutral flow over a ridge. *J. Atmos. Sci.,* **61,** in press.

Miloshevich, L. M., H. Vömel, A. Paukkunen, A. J. Heymsfield, and S. J. Oltmans, 2001: Characterization and correction of relative humidity measurements from Väisälä RS80-A radiosondes at cold temperatures. *J. Atmos. Oceanic Technol.,* **18,** 135–156.

——, A. Paukkunen, H. Vömel, and S. J. Oltmans, 2004: Development and validation of a time-lag correction for Vaisala radiosonde humidity measurements. *J. Atmos. Oceanic Technol.,* **21,** 1305–1327.

Neiman, P. J., F. M. Ralph, A. B. White, D. E. Kingsmill, and P. O. G. Persson, 2002: The statistical relationship between upslope flow and rainfall in California's coastal mountains: Observations during CALJET. *Mon. Wea. Rev.,* **130,** 1468–1492.

——, P. O. G. Persson, F. M. Ralph, D. P. Jorgensen, A. B. White, and D. E. Kingsmill, 2004: Modification of fronts and precipitation by coastal blocking during an intense landfalling winter storm in Southern California: Observations during CALJET. *Mon. Wea. Rev.,* **132,** 242–273.

Nieman, S. J., W. P. Menzel, C. M. Hayden, D. Gray, S. T. Wanzong, C. S. Velden, and J. Daniels, 1997: Fully automated cloud-drift winds in NESDIS operations. *Bull. Amer. Meteor. Soc.,* **78,** 1121–1133.

Nordø, J., and K. Hjortnæs, 1966: Statistical studies of precipitation on local, national, and continental scales. *Geofys. Publ.,* **26,** 1–46.

Overland, J. E., and N. A. Bond, 1995: Observations and scale analysis of coastal wind jets. *Mon. Wea. Rev.,* **123,** 2934–2941.

Ralph, F. M., and Coauthors, 1999: The California Land-falling Jets Experiment (CALJET): Objectives and design of a coastal atmosphere–ocean observing system deployed during a strong El Niño. Preprints, *Third Symp. on Integrated Observing Systems*, Dallas, TX, Amer. Meteor. Soc., 78–81.

——, and Coauthors, 2003: The impact of a prominent rain shadow on flooding in California's Santa Cruz Mountains: A CALJET case study and sensitivity to the ENSO cycle. *J. Hydrometeor.,* **4,** 1243–1264.

——, P. J. Neiman, G. A. Wick, and C. S. Velden, 2004: Satellite and CALJET aircraft observations of atmospheric rivers over the eastern North Pacific Ocean during the winter of 1997/98. *Mon. Wea. Rev.,* **132,** 1721–1745.

Rasmusson, E. M., 1985: El Niño and variations in climate. *Amer. Sci.,* **73,** 168–177.

——, and J. M. Wallace, 1983: Meteorological aspects of the El Niño/Southern Oscillation. *Science,* **222,** 1195–1202.

Reynolds, D. W., and A. P. Kuciauskas, 1988: Remote and in situ observations of Sierra Nevada winter mountain clouds: Relationships between mesoscale structure, precipitation, and liquid water. *J. Appl. Meteor.,* **27,** 140–156.

Rotunno, R., and R. Ferretti, 2001: Mechanisms of intense Alpine rainfall. *J. Atmos. Sci.,* **58,** 1732–1749.

Sawyer, J. S., 1956: The physical and dynamical problems of orographic rainfall. *Weather,* **11,** 375–381.

Smith, R. B., 1979: The influence of mountains on the atmosphere. *Advances in Geophysics*, Vol. 21, Academic Press, 87–230.

Szunyogh, I., Z. Toth, A. V. Zimin, S. J. Majumdar, and A. Persson, 2002: Propagation of the effect of targeted observations: The 2000 Winter Storm Reconnaissance Program. *Mon. Wea. Rev.,* **130,** 1144–1165.

Velden, C., and D. Stettner, 2001: GWINDEX—GOES Rapid-scan Winds Experiment: Applications for West Coast forecasting. Preprints, *14th Conf. on Numerical Weather Prediction*, Fort Lauderdale, FL, Amer. Meteor. Soc., 259–262.

——, C. M. Heyden, S. J. Niemea, W. P. Menzel, S. Wanzong, and J. S. Goerss, 1997: Uppe-tropospheric winds derived from geostationary satellite water vapor observations. *Bull. Amer. Meteor. Soc.,* **78,** 173–195.

Wang, J., 2005: Evaluation of the dropsonde humidity sensor using data from DYCOMS-II and IHOP_2002. *J. Atmos. Oceanic Technol.,* **22,** 247–257.

——, H. L. Cole, D. J. Carlson, E. R. Miller, K. Beierle, A. Paukkunen, and T. K. Laine, 2002: Corrections of humidity measurement errors from the Väisälä RS80 radiosonde—Application to TOGA COARE data. *J. Atmos. Oceanic Technol.,* **19,** 981–1002.

Webb, R. H., and J. L. Betancourt, 1992: Climate variability and flood frequency of the Santa Cruz River, Pima County, Arizona. U.S. Geological Survey Water-Supply Papers 2379, 40 pp.

White, A. B., J. R. Jordan, B. E. Martner, F. M. Ralph, and B. W. Bartram, 2000: Extending the dynamic range of an S-band radar for cloud and precipitation studies. *J. Atmos. Oceanic Technol.,* **17,** 1226–1234.

——, D. J. Gottas, E. Strem, F. M. Ralph, and P. J. Neiman, 2002: An automated brightband height detection algorithm for use with Doppler radar vertical spectral moments. *J. Atmos. Oceanic Technol.,* **19,** 687–697.

——, P. J. Neiman, F. M. Ralph, D. E. Kingsmill, and P. O. G. Persson, 2003: Coastal orographic rainfall processes observed by radar during the California Land-falling Jets Experiment. *J. Hydrometeor.,* **4,** 264–282.

Wolter, K., and M. S. Timlin, 1993: Monitoring ENSO in LOADS with a seasonally adjusted principal component index. *Proc. 17th Climate Diagnostics Workshop*, Norman, OK, NOAA/NMC/CAC, 52–57.

——, and ——, 1998: Measuring the strength of ENSO events: How does 1997/98 rank? *Weather,* **53,** 315–324.

Zhu, Y., and R. E. Newell, 1998: A proposed algorithm for moisture fluxes from atmospheric rivers. *Mon. Wea. Rev.,* **126,** 725–735.